COATING OF $La_{1-x}Sr_xCo_{1-y}Fe_yO_{3-\delta}$ FILMS ON ZIRCONIA AND CGO (CERIUM GADOLINIUM OXIDE) BY ELECTROSTATIC SPRAY DEPOSITION (ESD)

A Thesis Submitted to
the Graduate School of Engineering and Sciences of
İzmir Institute of Technology
in Partial Fulfillment of the Requirements for the Degree of

MASTER OF SCIENCE

in Materials Science and Engineering

by
Hande BÜYÜKKEBABÇI

December 2010
İZMİR

We approve the thesis of **Hande BÜYÜKKEBABÇI**

_____
Prof. Dr. Sedat AKKURT
Supervisor

_____
Prof. Dr. Muhsin ÇİFTÇİOĞLU
Committee Member

_____
Prof. Dr. Mustafa GÜDEN
Committee Member

22 December 2010

_____
Assoc. Prof. Dr. Mustafa M. DEMİR
Head of the Department of
Materials Science and Engineering

_____
Prof. Dr. Sedat AKKURT
Dean of the Graduate School of
Engineering and Sciences

ACKNOWLEDGEMENTS

ABSTRACT

COATING OF $La_{1-x}Sr_xCo_{1-y}Fe_yO_{3-\delta}$ FILMS ON ZIRCONIA AND CGO (CERIUM GADOLINIUM OXIDE) BY ELECTROSTATIC SPRAY DEPOSITION (ESD)

In this study preparation and characterization of coating of $La_{0.6}Sr_{0.4}Co_{0.8}Fe_{0.2}O_{3-\delta}$ and $La_{0.6}Sr_{0.4}Co_{0.2}Fe_{0.8}O_{3-\delta}$ materials on TZ-3Y (3 mol % doped yttria) and CGO ($Ce_{0.9}Gd_{0.1}$Oxide) ceramic electrolytes was studied. Electrostatic spray deposition (ESD) was used for depositing the coatings on ceramic electrolytes to develop a well bonded electrolyte-cathode material for potential IT-SOFCs (intermediate temperature solid oxide fuel cells) applications. Precursor solutions having $La_{0.6}Sr_{0.4}Co_{0.8}Fe_{0.2}O_{3-\delta}$ or $La_{0.6}Sr_{0.4}Co_{0.2}Fe_{0.8}O_{3-\delta}$ stoichiometry were prepared from various salts before being sprayed on a heated ceramic substrate which rapidly evaporated the solvent in the salts and the droplets struck and covered its surface. A high voltage was maintained to accelerate the droplets to high speeds. A coating with a minimal 1 μm of thickness was successfully produced. Effects of experimental parameters like the flow rate of the solution (0.3-1.5 ml/h), distance between the nozzle and substrate (15-45 mm), temperature of the substrate (250-375 °C), post heat treatment temperature (900-1300 °C) of the coated substrate and applied voltage on the quality of the coating were studied. Analytical tools like DTA/TGA, Scanning Electron Microscopy (SEM) and X-ray Diffraction (XRD) were used to investigate the samples to check for the quality of the coating. Coating microstructures ranged from dense to porous depending on the deposition parameters. Sample with 30 mm distance and 0.7 ml/h of flow rate produced the best reticulated structure of the coating. No preferential landing effect was observed on any of the samples studied. Zirconia was not an effective substrate for formation of $La_{0.6}Sr_{0.4}Co_{0.8}Fe_{0.2}O_{3-\delta}$ or $La_{0.6}Sr_{0.4}Co_{0.2}Fe_{0.8}O_{3-\delta}$. Cerium gadolinium oxide, however, was effective for $La_{0.6}Sr_{0.4}Co_{0.8}Fe_{0.2}O_{3-\delta}$ but not for $La_{0.6}Sr_{0.4}Co_{0.2}Fe_{0.8}O_{3-\delta}$.

ÖZET

ELEKTROSTATİK SPREY KAPLAMA (ESD) METODU İLE ZİRKONYA VE CGO (SERYUM GADOLİNYUM OKSİT) ÜZERİNE $La_{1-x}\,Sr_xCo_{1-y}Fe_yO_{3-\delta}$ FİLMLERİNİN KAPLANMASI

Bu tezde $La_{0.6}Sr_{0.4}Co_{0.8}Fe_{0.2}O_{3-\delta}$ ve $La_{0.6}Sr_{0.4}Co_{0.2}Fe_{0.8}O_{3-\delta}$ katot malzemelerinin TZ-3Y (% 3 mol yitriya katkılı zirkonya) ve CGO seramik elektrolitlerinin üzerine kaplanmasının karakterizasyonu çalışılmıştır. Orta sıcaklıktaki katı oksit yakıt hücelerine uyumlu katot ve elektrolit malzemesini geliştirebilmek için elektrostatik sprey kaplama tekniği kullanıldı. Çeşitli metalik tuzlar kullanılarak $La_{0.6}Sr_{0.4}Co_{0.8}Fe_{0.2}O_{3-\delta}$ veya $La_{0.6}Sr_{0.4}Co_{0.2}Fe_{0.8}O_{3-\delta}$ stokiyometrilerine sahip çözeltiler hazırlandı. Tuzların içinde çözündüğü bu çözeltiler, sıcak seramik yüzey üzerine püskürtüldü ve böylece seramik yüzey kaplandı. Püskürtme sırasında tanelere yüksek voltaj uygulandı. 1 μm kalınlığında kaplamalar elde edildi. Çözeltinin akış oranı (0.3-1.5 ml/h), püskürtücü başlık ile seramik yüzey arasındaki uzaklık (15-45 mm), yüzey sıcaklığı (250-375 ^{o}C), kaplanmış yüzeylerin ısıl işlemi (900-1300 °C) ve uygulanan voltaj gibi deneysel parametrelerin etkisi çalışıldı. Numuneler DTA/TGA, taramalı electron mikroskop ve X ışınları analizi kullanılarak incelendi. Kaplanan mikroyapıların özellikleri kaplama parametrelerine bağlı olarak yoğun ve poroz olarak çeşitlendi. 30 mm uzaklık ve 0.7 ml/h akış oranına sahip olan en iyi ağ şeklindeki mikroyapı elde edildi. Hiçbir numunede tanelerin üst üste binme etkisi gözlenmedi. % 3 mol yitriya katkılı zirkonya seramik yüzeyi $La_{0.6}Sr_{0.4}Co_{0.8}Fe_{0.2}O_{3-\delta}$ ve $La_{0.6}Sr_{0.4}Co_{0.2}Fe_{0.8}O_{3-\delta}$ katot üretimi için kullanışlı değildir. Fakat seryum gadolinyum oksit seramik yüzey ise sadece $La_{0.6}Sr_{0.4}Co_{0.8}Fe_{0.2}O_{3-\delta}$ katot malzeme üretimi için kullanışlıdır.

TABLE OF CONTENTS

LIST OF FIGURES

LIST OF TABLES

CHAPTER 1

INTRODUCTION

Fuel cells can generate energy from fossil fuels more efficiently and more benignly than other alternatives. They convert chemical fuel into electrical energy by an electrochemical system without combustion of the fuel at high temperature. Hence, no environmentally hazardous emissions are produced. The principle of operation of fuel cells is simple. Fuel (hydrogen) and oxygen are fed from the two sides of an electrolyte through which oxygen ions pass to the other side of the electrolyte. Electrons are produced at the anode and consumed at the cathode while producing an electrical potential energy. William Grove demonstrated the basic operating principle of fuel cells in 1839 (Hoogers et al., 2003). The principle involved reversing water electrolysis to generate electricity from hydrogen to oxygen. Studies on converting chemical energy into electricity started around 1900s and then in the 1960s NASA projects on fuel cells in the USA was an important step in this area (Venkatasubramanian, 2003).

Fuel cells are usually classified according to the nature of the electrolyte which runs at the optimum temperature. Fuel cells are generally named after the type of the electrolyte. For example, AFC (Alkaline Fuel Cell), PAFC (Phosphoric Acid Fuel Cell), MCFC (Molten Carbonate Fuel Cell), SOFC (Solid Oxide Fuel Cells), PEMFC (Proton Exchange Membrane Fuel Cell or Polymer Electrolyte Fuel Cell) and DMFC (Direct Methanol Fuel Cell) (Ecn, 2010).

In the scope of this thesis an SOFC system is studied. An SOFC is composed of two porous electrodes (anode and cathode) interposed between them is an electrolyte made of a dense solid oxide ceramic material. The cathode and anode electrodes show electronic and ionic conductivity (Huijmans et al., 2001). The electrolyte in this fuel cell is a solid, nonporous metal oxide, usually Y_2O_3 stabilized ZrO_2 (YSZ). The cell operates at around 1000 °C where ionic conduction by oxygen ions takes place. Typically, the anode is Ni-ZrO_2 cermet and the cathode is Sr doped $LaMnO_3$ (LSM) (EG&G Technical Services, 2004).

A number of activities are concerned with the optimisation and development of cell materials and microstructures with the aim of reducing the solid oxide fuel cell

(SOFC) operating temperature down from 1000 °C (Huijmans et al., 1998). This group of SOFC is called intermediate temperature solide oxide fuel cells (IT-SOFC) which are better the lower the operating temperature. One of the most important reasons for lowering the temperature is the reduced cost of the system. Moreover, the use of lower temperature can increase the lifetime of the fuel cell (Marinha et al., 2009). Decreasing the operating temperature leads to increased ohmic losses. To minimize the ohmic drop through the electrolyte research efforts are underway (Wilhelm et al., 2005). The development of new electrolytes with high ionic conductivity as well as efforts to reduce the thickness of the electrolyte are tested to decrease the ohmic resistance (Steele et al., 2000). Scandia stabilized zirconia (ScSZ) (Yamamato et al., 1998), TZ-2Y (Nguyen et al., 2001), Cerium gadolinium oxide (CGO) (Taniguchi et al., 2003; Marinha et al., 2009, respectively) are examples for tests on different electrolyte materials in order to minimize the ohmic losses. The cathode material used in the electrode naturally depends on the type of the electrolyte material. Therefore for SOFC material development, the whole system should be considered, not the performance of individual components (Tietz et al., 2008). Significant expertise is built now on the assembly of these components into an SOFC stack which produces the desired power (Ecn, 2010).

In this thesis, the deposition of LSCF cathode material on CGO and yttria doped 3% mol zirconia (TZ-3Y) electrolyte was tested. The deposition of LSCF cathode material on CGO was investigated earlier by Taniguchi et al and Marinha et al like mentioned above (Taniguchi et al., 2003; Marinha et al., 2009). In addition, LSCF films coated on either TZ-3Y or CGO were compared in this study.

Electrostatic spray deposition (ESD) is a modern technique of depositing films on substrates. This process provides many advantages: experimental devices are simple and inexpensive, a wide range of precursor, depositing, a good control of morphology and stoichiometric deposited layers. Moreover, the depositing process can be done under air. In chapter 2 of this thesis, a description of the principle operation of ESD, its scope and processes on deposits of TZ-3Y and CGO will be presented. The experimental procedure and the results of this study are given and discussed in Chapters 3 and 4, respectively, while the conclusions are stated in the last chapter.

CHAPTER 2

LITERATURE SEARCH

2.1. Fuel Cells

Worldwide efforts to commercialize SOFCs involve numerous investigation. Complete cells for SOFC typically are produced by one method: electrolyte supported cells in which an electrolyte foil carries an anode and a cathode on opposing sides (Primdahl et al., 2000).

A fuel cell is an electrochemical cell, which can convert the chemical energy of a fuel and an oxidant to electrical energy by a process involving electrode-electrolyte system. The chemical energy is provided by a fuel and an oxidant stored outside the cell in the fuel cell. Electricial energy is produced continuously as long as this cycle continues (Venkatasubramanian, 2003). In case of effcient, clean, modular and reliable nature of fuel cells makes them interesting candidates for energy generation (Bauen et al., 2000). Although fuel cells show some similarities with batteries, fuel cell do not need recharging, but not batteries (Hoogers et al., 2003). Fuel cells are capable of converting 40 % of the available fuel to electricity. This can be raised to 80 % with heat recovery. The fuel cell itself has no moving parts, offering a quiet and reliable source of power. (EG&G Technical Services, 2004).

Fuel cells use common fuels or hydrogen as a reductant and air as the oxidant though fuel cells has a wide variety of fuels and oxidants (EG&G Technical Services, 2004). Because, hydrogen has can be obtained from common fuels such as hydrocarbon, alcohols or coal. Oxygen is the most common oxidant because it is economically available from air (Minh et al., 1995). In Figure 2.1, a fuel cell can be seen schematically.

Most fuel cell systems contain:

I. Fuel preparation. Except when pure fuels (such as hydrogen) are used, some fuel preparation is required, usually involving the removal of impurities and thermal conditioning.

II. Air supply. In most practical fuel cell systems, this includes air compressors or blowers as well as air filters.

III. Thermal management. All fuel cell systems require careful management of the fuel cell stack temperature.

IV. Water management. Water is needed in some parts of the fuel cell, while overall water is a reaction product (EG&G Technical Services, 2004).
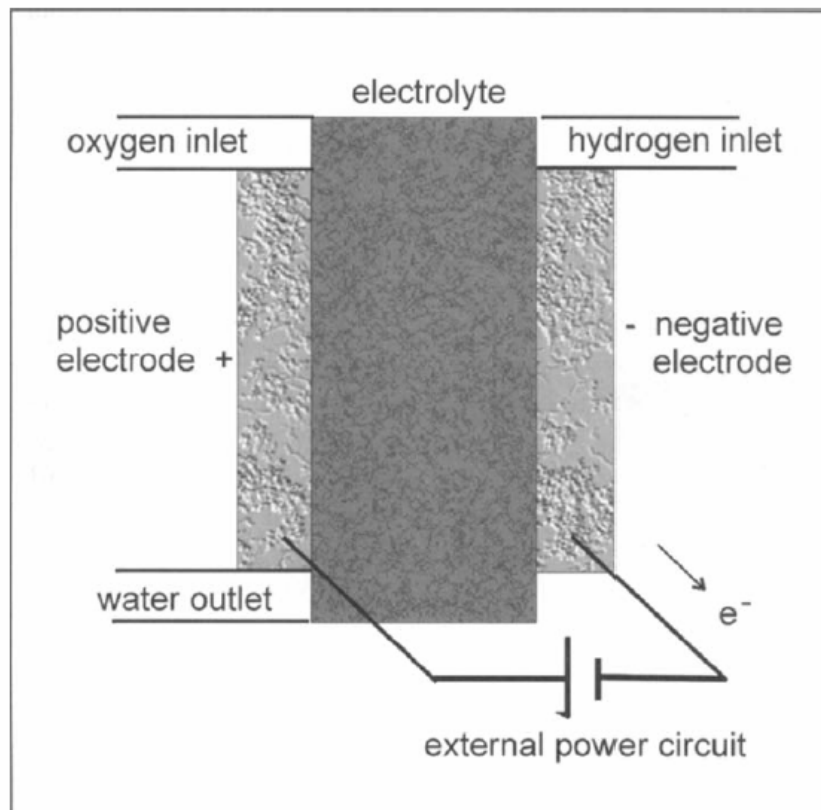
Figure 2.1. Schematic picture of a fuel cell
(Source: Sørensen, 2005)

2.1.1. Fuel Cell Types

There are many different types of fuel cells. These can distinguish by commerce area, degree of suitability for applications and material costs (Larminie et al., 2003). Moreover, fuel cells vary according to using electrolyte and applying temperature. Table 2.1 shows the different types of fuel cells along with electrolyte used, operating temperature and electrode reactions.

Each type of fuel cell has some advantages and disadvantages. For example, alkaline fuel cells allow the use of nonprecious metal catalysts but suffer from the problem of liquid electrolyte management and electrolyte degradation. Molten carbonate fuel cells can tolerate high concentrations of carbon monoxide in the fuel stream (CO is a fuel for such fuel cells), but their high operating temperature precludes rapid start-up and sealing remains an issue (Ramani, 2006). Polymer electrolyte cells work at quite low temperature, so the problem of slow reaction rates is addressed. Direct methanol fuel cells use methanol as the fuel. Solid oxide fuel cells offer high performance owing to operating in the region of 600-1000 °C. In this way, high reaction rates can be achieved without expensive catalysts (Larminie et al., 2003). However, higher temperatures are necessary for the electrolytes to be sufficiently conductive to sustain fuel cell operation at reasonable power levels. Hence, these systems suffer from materials related problems such as system cost and lifetime (Rosa et al., 2009).

Table 2.1. Classification of fuel cells
(Source: Ramani, 2006)

Fuel Cell Type	Electrolyte Used	Operating Tempearture		Electrode Reactions
Polymer Electrolyte	Polymer Membrane	60-140°C	Anode:	$H_2 = 2H^+ + 2e^-$
			Cathode:	$^1/_2 O_2 + 2H^+ + 2e^- = H_2O$
Direct Methanol	Polymer Membrane	30-80°C	Anode:	$CH_3OH + H_2O = CO_2 + 6H^+ + 6e^-$
			Cathode:	$^3/_2 O_2 + 6H^+ + 6e^- = 3H_2O$
Alkaline	Potassium Hydroxide	150-200°C	Anode:	$H_2 + 2 OH^- = H_2O + 2e^-$
			Cathode:	$^1/_2 O_2 + H_2O + 2e^- = 2 OH^-$
Phosphoric Acid	Phosphoric Acid	180-200°C	Anode:	$H_2 = 2H^+ + 2e^-$
			Cathode:	$^1/_2 O_2 + 2H^+ + 2e^- = H_2O$
Molten Carbonate	Lithium/Potassium Carbonate	650°C	Anode:	$H_2 + CO_3^{2-} = H_2O + CO_2 + 2e^-$
			Cathode:	$^1/_2 O_2 + CO_2 + 2e^- = CO_3^{2-}$
Solid Oxide	Yittria Stablized Zirconia	1000°C	Anode:	$H_2 + O^{2-} = H_2O + 2e^-$
			Cathode:	$^1/_2 O_2 + 2e^- = O^{2-}$

2.1.1.1. Solid Oxide Fuel Cells (SOFCs)

As can be seen in Figure 2.2, a solid oxide fuel cell (SOFC) is typically composed of an electrolyte made of a solid oxide ceramic material and two porous electrodes, the anode and cathode. (Sammes et al., 2006). While hydrogen is being fed to anode material, oxygen is fed to cathode material.
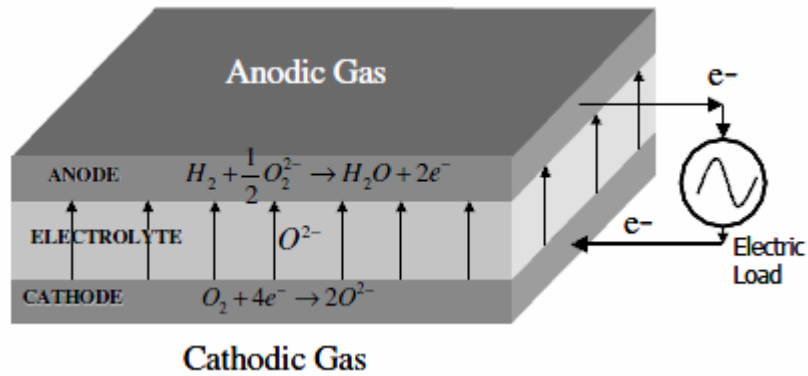
Figure 2.2. Schematic picture of a solid oxide fuel cell
(Source: Sammes et al., 2006)

Thanks to cathode and anode porous materials, oxygen ions migrate from the cathode to the anode. At this time the reduction of oxygen occurs at the cathode. At the anode, oxygen ions reacts with hydrogen and produce water as can be seen these steps in equations 2.2, 2.3 and 2.4. As reaction occurs, electrons are released at the anode and migrate from the cathode to an external electric circuit. In this way, an electric current generate (Sammes et al., 2006).

$$O_2 + 4e^- \rightarrow 2O^{2-} \qquad (2.2)$$

$$H_2 + O^{2-} \rightarrow H_2O + 2e^- \qquad (2.3)$$

$$H_2 + \frac{1}{2}O_2 \rightarrow H_2O \qquad (2.4)$$
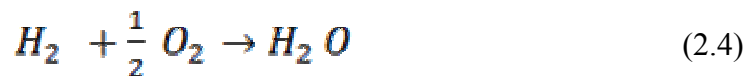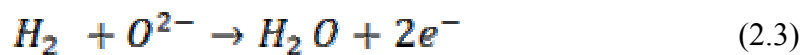
Some important properties are expected from fuel cells such as high conversion efficiency, enviromental compatibility and multifuel capability. When this properties is considering, ceramic fuel cells are appropriate devices because they prevent material corrosion and electrolyte management problems. Ceramic fuel cells are defined as SOFCs (Minh et al., 1995).

Energy conversion using SOFCs is a highly efficient and a benign technology for environmental. It reduces the emission of pollutants, such as NO_x, SO_x, CO_2 and dust. However, the development of SOFC for efficient power generation has still failed to reach commercial viability because of high operating temperature SOFCs and due to

6

the longterm degradation problems. Therefore, the development of intermediate-temperature SOFCs (IT-SOFCs) has been started at 500-700 °C. Since the operation at intermediate temperatures causes an increase in the interfacial polarization losses of a solid state cell, as well as ohmic loss in the electrolyte, the performance of IT-SOFCs is strongly dependent on both the electrolyte and the cathode electrolyte interface (Taniguchi et al., 2003).

Ohmic losses can be described by Ohm's law. The correlation between voltage and current can be explained by resistivity. Hence, oxygen ions transition from the cathode to the electrolyte and transition of electrons through the cathode to the anode are run by ionic resistivity and electronic resistivities, respectively. Owing to these ohmic resistances at a given current, there is a voltage losses.

The electrolyte causes more ohmic losses, especially in thick electrolyte supported cells in IT-SOFCs because, ionic resisitivity of the electrolyte is greater than electronic resistivity of the cathode and the anode. That is why, electrolyte material which has high ionic conductivity has been searched (Singhal et al., 2003).

Polarization losses are associated with the electrochemical reactions taking place at the interface between the electrodes and the electrolyte. The kinetics of the electrode reactions (equations 2.2 and 2.3) play significant role in determining polarizaiton losses in SOFCs. In practical applications, SOFCs may use gaseous mixtures that contain. For example, coal gas and natural gas in addition to hydrogen. These gas mixtures may contain sulfide impurities and the presence of significant levels of sulfur may cause an unacceptable loss of cell voltage (Singhal et al., 2003).

The operation of a SOFC is based on electrical conduction in the ceramic components. The electrolyte conducts ions between the anode and cathode. Therefore, electrical conduction processes in ceramics are important for the operation of the SOFC. Emphasis is placed on the discussion of electrical conduction perovskite oxides which is the common type of oxide used in SOFCs. Perovskite type oxides of general formula is ABO_3, A is a large cations, B is a small cations (Singhal et al., 2003). These perovskites are used as cathode material for ceramic fuel cells. (Minh et al., 1995).
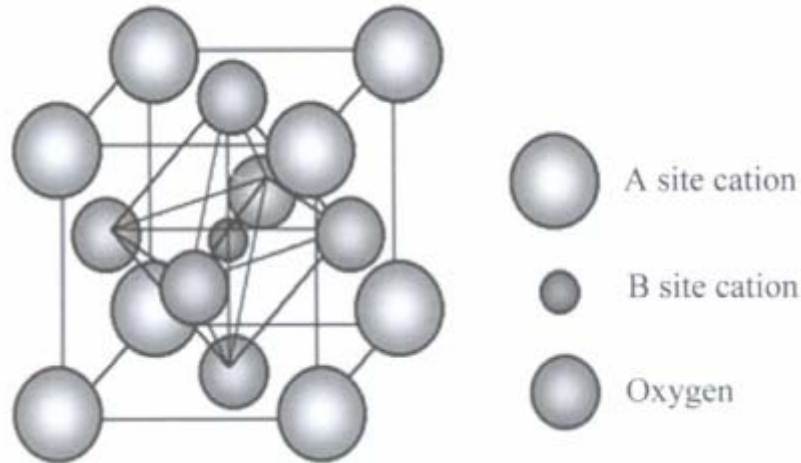
Figure 2.3. Schematic representation of structure of perovskite (ABO_3)
(Singhal et al., 2003)

2.1.1.1.1. Electrolytes

The electrolyte must be chemically and morphologically stable both reducing and oxidizing environments and must have high ionic conductivity. Its ionic conductivity must be as high as possible to minimize ohmic losses. The electrolyte must possess low electronic conductivity to prevent voltage losses because of the electronic current flowing through the electrolyte for SOFCs (Minh et al., 1995). Generally, yttria stabilized zirconia (YSZ) which has fluorite structure, has been the most favoured electrolyte. Pure ZrO_2 exhibits negligible ionic conductivity at 1000°C. However, doping with several percent of a lower valent metal oxide Y_2O_3, considerably improves the situation. For example, since the excess charge introduced Y^{3+} onto Zr^{4+} sites are compensated by oxygen vacancies, the high vacancy concentration leads to an ionic conductivity of 0.1 S/cm at 1000 °C for a Y_2O_3 content of 8 mol %. Therefore YSZ are often used (Fleig et al., 2003).

Moreover, doped ceria electrolyte materials which has generally fluorite structure and also perovskite and hexagonal structure are used for SOFCs (Ishihara et al., 1994). At 1000 °C, CeO_2 doped with 10 % Gd exhibits (CGO) a conductivity of 0.25 S/cm which exceeds that of zirconia (Fleig et al., 2003). CGO achieves the required conductivity at 500 °C and therefore could be used in IT-SOFC operating at this temperature (Nicholas et al., 2007).

2.1.1.1.2. Cathodes

Cathodes have to possess many properties such as high electrical conductivity to support electron flow in oxidizing environment. Also cathodes must be compatible with other components and interdiffusion between the cathode and adjacent components must be limited to avoid unacceptable formation as secondary phases. In order to allow gas transport, cathodes must have porosity structure (Minh et al., 1995).

Platinum was used in the early stages as cathode for SOFC development, since it is expensive, it is not appropriate. Then the first perovskite $LaCoO_3$ was studied by Tedmon et al. Because of some problems, investigation of cathode materials were continued. Lanthanum manganite was tried (Minh et al., 1995). $LaMnO_3$ is one of the typical cathode materials (Fleig et al., 2003). Strontium doped lanthanum manganite (LSM) is shown good performance for cathode material (Larminie et al., 2003). Perovskite structured oxides that exhibit high ionic conductivity have attracted considerable attention due to their various applications in IT-SOFCs (Yashima et al., 2008). Therefore, the Sr and Fe co-doped lanthanum cobaltites (LSCF) perovskite material has been developed for especially intermediate temperature (IT) SOFCs (Han et al., 1993). $La_{1-x}Sr_xCo_{1-y}Fe_yO_{3-\delta}$ (LSCF) perovskite materials offer high electronic and ionic conductivities. These important properties make possible applications of LSCF perovskites as cathodes for solid oxide fuel cells operating temperatures (700–800 °C) are preferred (SOFC) (Petric et al., 2000).

2.1.1.1.3. Anodes

The anode must combine catalytic activity with electrical conductivity. Catalytic properties of anode are necessary for the fuel oxidation with the oxide ions coming through the solid electrolyte. Also, ionic conductivity allows the anode to spread the oxide ions and electrical conductivity must be to convey the electrons resulting from the electrode reaction out into the external circuit (Singhal et al., 2003). The Ni/YSZ cermet anode used by most SOFC developers commonly is produced by reducing an NiO/YSZ anode. The anode must have sufficient porosity to allow gas transport to the reaction sites (Minh et al., 1995).

2.1.1.1.4. SOFC Materials

Desired characteristics properties for using materials consist of chemical stability under the operational conditions, high electrical conductivity for the electrodes and electrical interconnects, high ionic conductivity and almost zero electrical conductivity for the electrolyte and low cost (Sammes et al., 2006). TZ-3Y (TOSOH) with uniform dispersion of 3 mol % yttria and cerium gadolinium oxide ($Ce_{0.9}Gd_{0.1}Oxide$) (PRAXAIR) powders were used as electrolyte in this thesis.

. TZ-3Y exhibits superior sintering properties and higher aging resistance. TZ-3Y show a fine crystal grain structure resulting in great improvements in strength, fracture toughness, as well as resistance to wear and aging. Because of these properties, TZ-3Y is good choice for SOFC (Tosoh, 2010).

Ceria based ceramics are ionic conductors and are highly oxygen conductive when subjected to temperatures of around 600 °C. Therefore, it is desirable to reduce SOFC operating temperature to an intermediate temperature, while still maintaining the power density achieved at high temperature (Laukaitis et al., 2007).

2.2. Electrostatic Spray Deposition (ESD)

Electrostatic spray deposition (electrohydrodynamic spraying) is a method of liquid atomization by means of electrical forces (Jaworek et al., 2008). Electrostatic spray deposition technique compared to other film deposition techniques bears the advantage of high deposition efficiency (up to 80 %) as the droplets are transported by electrical forces (Siefert et al., 1984). The schematics of the ESD set-up are presented in Figure 2.3. A precursor solution is atomized by an electric field to an aerosol which is then directed to a heated substrate where a thin film is deposited. This process is well appropriated to deposit nanostructured thin and dense electrolyte films and nanostructured cathode films with controlled microstructures (Princivalle et al., 2008).

ESD system have several advantages. The droplet sizes of electrospraying can range from hundreds micrometers down to several tens of nanometer. The size distribution of the droplets can be nearly monodisperse. Droplet generation and droplet size can be controlled to some extent via the flow rate of the liquid and the voltage at the capillary nozzle. The fact that the droplets are electrically charged facilitates control

of their motion (including their deflection and focusing) by means of an electric field (Jaworek et al., 2008). In addition, the process has very simple set-up, low cost and working under air (Marinha et al., 2009).
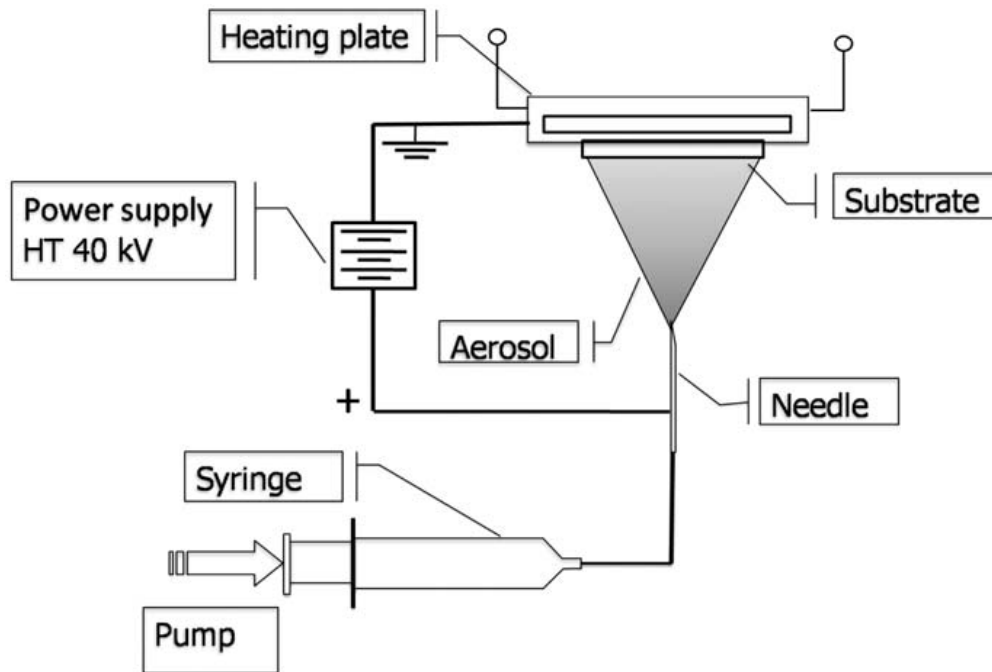
Figure 2.4. Schematic ESD process
(Source: Neagu et al., 2005)

Spray modes is significant to obtain homogeneous structure. The precursor solution can be atomised in many different spray modes. Basically, a liquid is forced to flow through a metal nozzle which is subjected to an electric field, the liquid will leave the outlet of the nozzle in different modes (Chen, 1998). Types of spray modes depend on the applied voltage, the flow rate, and the physical properties of the liquid. Several attempts have been undertaken to classify the modes of electrostatic spraying. In Figure 2.5, some different types of modes can be seen. Usually the cone jet mode is preferred, because it produces single-sized droplets in the range of several micrometers (Neagu, 2005). In the among the different cone jets, single jet mode is more appropriate than the others, because the cone with a straight generatrix is called Taylor cone with 49.3 ° half angle at the apex of the cone (Chen, 1998).
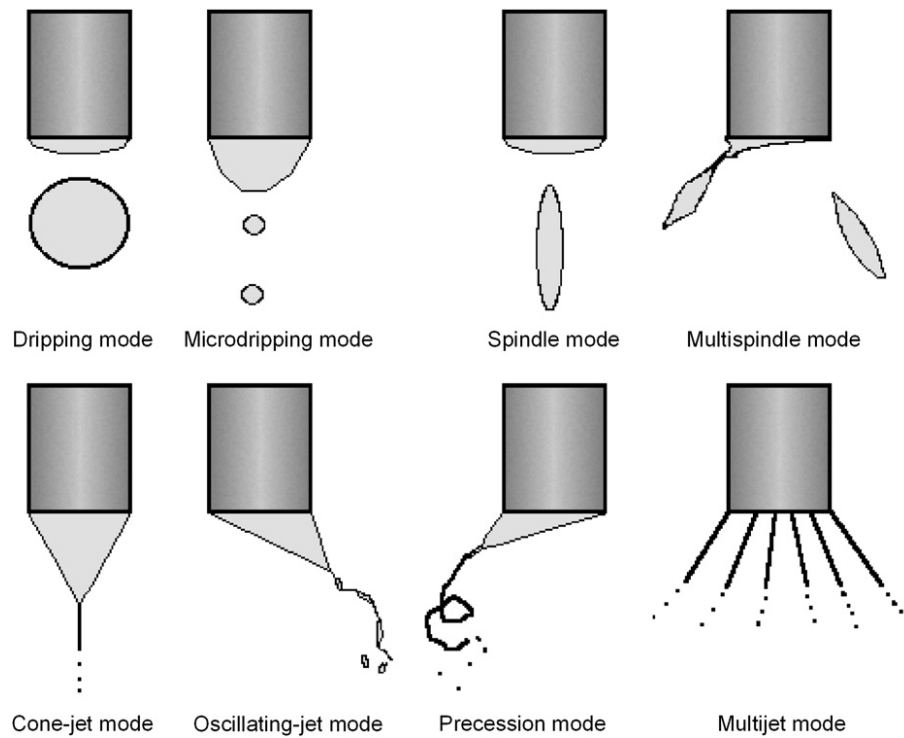
Figure 2.5. Various modes of electrospraying
(Source: Jaworek et al., 2008)

In ESD process, possible sequential steps are shown in Figure 2.6. These are investigated.

sequence: 1 - 2 - 3 - 4 - 5
1: spray formation
2: droplet transport, evaporation, disruption
3: preferential landing
4: droplet spreading, penetration, drying
5: surface diffusion, reaction
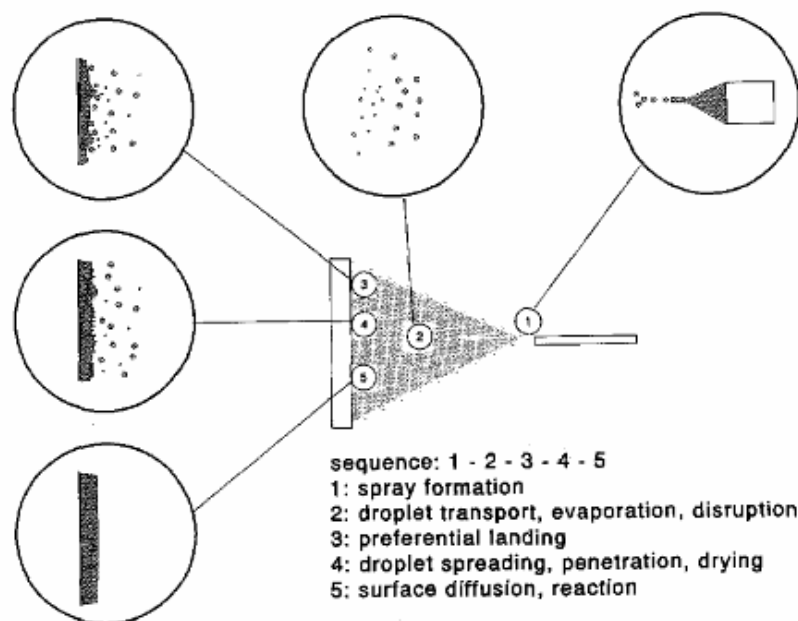
Figure 2.6. The steps of ESD process
(Source: Chen, 1998)

2.2.1. Spray Formation

The precursor solution is placed in a syringe which is connected to a metal capillary tube. When a voltage is applied to the capillary, an electrostatic field is immediately set up across the capillary and plate. This field penetrates the liquid surface and acts on ions in the solution.

2.2.2. Droplet Transport, Evaporation and Disruption

During the flight Charged droplets will be attracted towards a grounded substrate by three forces;

i.   a Coulomb force (F = q· Er) q is droplet charge and E is electric field strength

ii. a gravitational force (G = mg) m is the mass of the droplet and g is gravitational acceleration constant

iii. a drag force (F = d · η · v · C) η is the dynamic viscosity of air, v is the drop velocity and C is a correction coeffcient.

Actually, the real situation is further complicated from theoretical situation and these factors the flight speed and time.

Alcohol solutions are used generally in the ESD process. Solvent evaporation during the flight of a solution droplet is inevitable. The disruption of a droplet usually occurs with the ejection of a few highly charged. Therefore, the evaporation and disruption can be change according to volatile alcohols as solvent, nozzle to substrate distance and deposition temperature (Chen, 1998).

2.2.3. Preferential Landing of Droplets

Charged droplets exist on the substrate generally is not uniform in the strong electrostatic field or at high temperature. They tend to teh effect of preferential landing (Marinha et al., 2009). The charged droplets go at the places where the curvature is greater. Therefore when a droplet approaches the surface, it will be tend to more curved areas (Chen, 1998). In this way, preferential landing effect will be shown.

2.2.4. Droplet Spreading and Drying

Spreading of droplet is significant another parameter for ESD technique. The shape of the liquid surface during spreading, and the size of the final splat depend on the size and velocity of the droplet, properties of the liquid viscosity and the contact angle between the substrate and the liquid. Figure 2.5 shows a possible sequence from the impacting droplet to the equilibrium meniscus (Neagu, 2005).
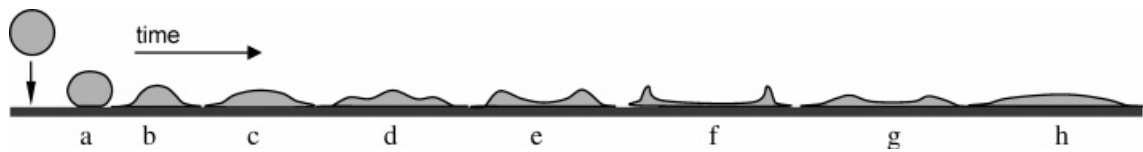
Figure 2.7. A liquid droplet spreading on a flat, smooth surface
(Source: Marinha et al., 2009)

2.2.5. Surface Diffusion, Reaction

In the droplets may have occured the reaction before the droplets reach the substrate if the temperature is high enough and dried droplets have been formed. The morphology of the formed droplets on the layer can be change with rate of spreading, precipitation, decomposition and reaction. For example, the solubilities of the salts in alcohol are large for the formation of a dense layer (Chen, 1998).

2.2.6. The Morphology Parameters

The microstructure depends on the ESD process parameters. Deposition temperature, nozzle to substrate distance, flow rate of precursors solution and the physical and chemical characteristics of the precursor solutions are some of parameters.

2.2.6.1. DepositionTemperature

The formation of coating is the result of the evaporation of the solvent in ESD process when the solvent reaches a hot substrate. Therefore, the temperature is an significant parameter because the evaporation rate of the solvent and precursor

decomposition depend on the temperature (Djurado et al., 2005).

2.2.6.2. Nozzle to Substrate Distance

Changing the nozzle to subsrate distance is associated with greater solvent evaporation because droplet takes longer time to reach the substrate.According to high or low distances, droplet size will be larger or slower and drier, respectively (Marinha et al., 2009). On the other hand, when same quantity of solution is sprayed to the substrate, droplet cover a larger area if the the distance is increased or vice versa (Djurado et al., 2005).

2.2.6.3. Precursor Solution Flow Rate

The precursor solution flow rate determines the amount of the liquid at the tip of the nozzle and thereby determines droplet size. When the amount of the accumulation liquid is increased, larged sized droplets will be generated. These droplets take longer time to dry (Marinha et al., 2009).

2.2.6.4 Precursors and Solvents

One of the advantages of the ESD technique is the largely choice of precursors. In order to prepare precursor solutions, some metallic nitrates and strontium chloride were used as salt and ethanol, butyl carbitol and water were used as solvents in this study. Some features of these salts and solvents are given Table 2.2.

In ESD process, precursors must be soluble in an alcohol solvent, it must be decomposed and converted into a desired product at the deposition temperature, it should not contaminant or impurity.

Moreover, a solvent must be proper physico- chemical properties for atomization of the precursor solution.

Table 2.2. Physical properties of the used salts

Materials	Molecular Weight (g/mol)	Melting Point (°C)	Decomposition Temperature (°C)	Density (g/cm^3)	Source
La(NO$_3$)$_3$ 6H$_2$O	433.0	40	700	2.05	Princivalle et al., 2004
SrCl$_2$ 6H$_2$O	266.6	570	220	1.93	Princivalle et al., 2004
Fe(NO$_3$)$_3$ 9H$_2$O	403.9	47	> 250	1.68	Elmasry, 1998
Co(NO$_3$)$_2$6H$_2$O	291.0	56	185	1.87	Ehrhardt, 2005
C$_2$H$_6$O	46.0	-114	78 (b.p.)[*]	0.78	Chen, 1998
C$_8$H$_{18}$O$_3$	162.2	-68	231(b.p.)	0.95	Chen, 1998
H$_2$O	18.0	0	100 (b.p.)	0.99	Chen, 1998

[*] b.p refer to boiling point

CHAPTER 3

EXPERIMENTAL

In this chapter, the materials used and the experimental procedure followed in this thesis were presented. The thesis is involved with the deposition and characterization $La_{0.6}Sr_{0.4}Co_{0.8}Fe_{0.2}O_{3-\delta}$ (LSCF-6482), $La_{0.6}Sr_{0.4}Co_{0.2}Fe_{0.8}O_{3-\delta}$ (LSCF-6428) and cathode films on zirconia TZ-3Y (doped with 3 mol. % Y_2O_3) and cerium gadolinium oxide ($Ce_{0.9}Gd_{0.1}$Oxide, CGO) electrolyte materials by using electrostatic spray deposition (ESD) technique. Here a ceramic disc of TZ-3Y or CGO is coated with a sprayed solution of cathode material (Figures 3.1 or 3.4). Below are given the chemicals used in the preparation of the solution and the ceramic substrate disc.
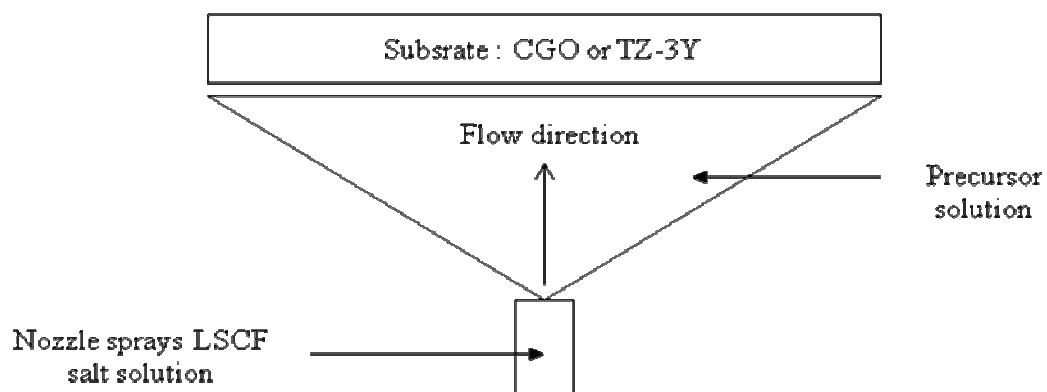
Figure 3.1. Simplified schematic of the coating process

3.1. Powder Properties

3.1.1. Powders Used in Preparation of Substrate

First of all, cerium gadolinium oxide ($Ce_{0.9}Gd_{0.1}$Oxide, PRAXAIR, 99.9 %) and zirconia TZ-3Y (doped with 3 mol. % Y_2O_3, TOSOH, 99.9 %) were used for preparing the substrate of ceramic electrolyte discs to be coated by the cathode materials.
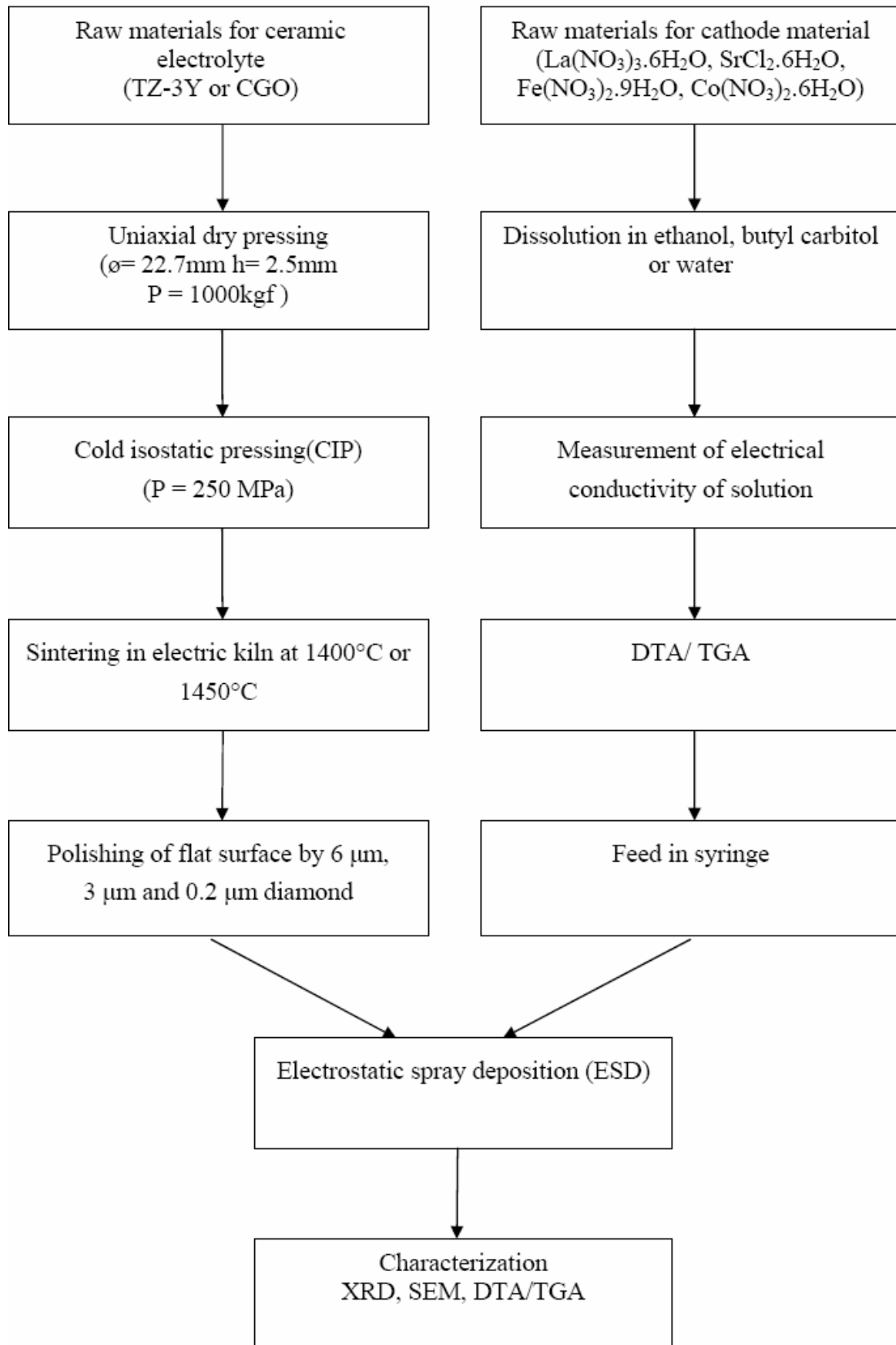
Figure 3.2. Flowchart of the experimental work followed in this thesis.

3.1.2. Precursor Solutions for Coating of Cathode

Precursor solutions were prepared from mixtures of lanthanum nitrate, hexahydrate (RECTAPUR, 99.99 %), iron III nitrate, nonahydrate (SIGMA-ALDRICH, 99.99 %), cobalt II nitrate, hexahydrate (SIGMA-ALDRICH, 99.999 %) and strontium chloride hexahydrate (STREM CHEMICALS, 99 %) salts. The solvents used for dissolving these salts were either ethanol (SIGMA-ALDRICH, 99.8 %) in water or diethylene glycol monobutyl ether (butyl carbitol, ACROS ORGANICS, 99+ %).

3.2. Method

3.2.1. Preparation of the Substrate

The CGO powders to be used for pellet preparation were first calcined (Carbolite Furnace HTC 1000) at 700 °C for 7 h. TZ-3Y and CGO powders were compacted by uniaxial pressing in a stainless steel die (Φ= 22.7mm) at 1000 kgf, then by CIP (Cold Isostatic Pressing) at 250 MPa (Figure 3.3). Samples were placed in a plastic bag under vacuum to avoid penetration of oil during the CIP process. The samples were sintered (Carbolite Furnace HTC 1500) at 1400 °C and 1450 °C for 2 and 4 hours in air, respectively. Heating rates were 1.6 and 5 °C/min respectively. The surfaces of all densified substrates were machined to produce a straight polished surface. 6 µm, 3 µm and 0.2 µm diamond suspensions were used in polishing to obtain uniform surface (Presi, Mecapol 200). Finally, samples around 19 mm of diameter and 1.2 mm of thickness, were obtained. These samples were then ready for ESD coating process.

3.2.2. Preparation of Precursor Solutions for Cathode

As can be seen in Figures 3.1, 3.4 and 3.5, a solution is sprayed up through a nozzle on the heated ceramic substrate. This solution is prepared from different salts to produce the final desired stoichiometry of the cathode. The weight of the precursor salt

for a particular component i is defined as m_i and is diluted in the solvent as determined using the following equation:

$$m_i = x_i \cdot M_i \cdot C \cdot V \qquad (3.1)$$

x_i: atomic fraction

M_i: molecular weight

C: concentration of solution (mol/L)

V: solution volume (L)
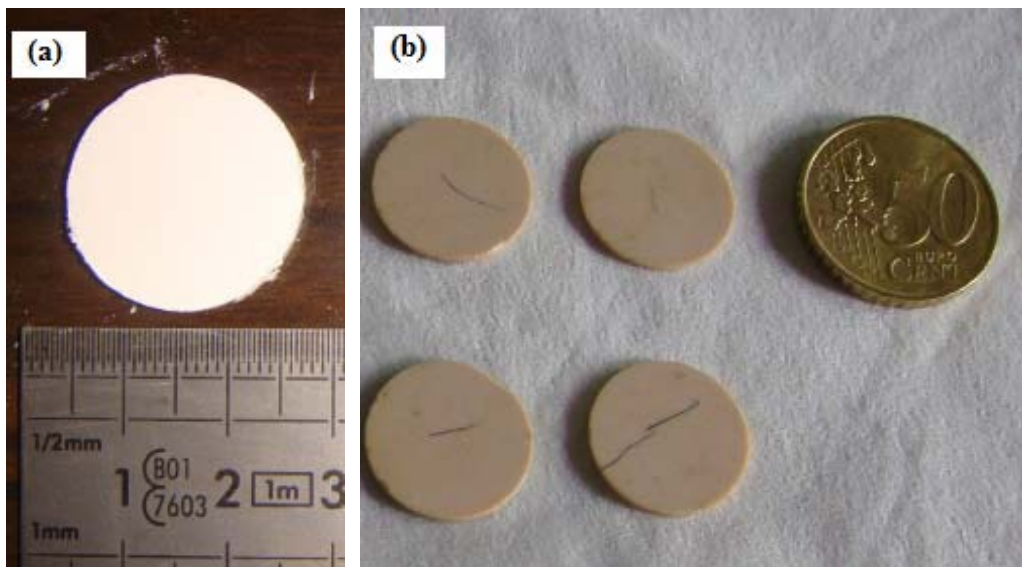
Figure 3.3. Samples of pressed ceramic electrolyte discs: (a) before and (b) after sintering

La(NO$_3$)$_3$.6H$_2$O, SrCl$_2$.6H$_2$O, Fe(NO$_3$)$_3$.9H$_2$O, Co(NO$_3$)$_2$.6H$_2$O were used as precursor salts. Ethanol (C$_2$H$_5$OH, SIGMA-ALDRICH), diethylene glycol monobutyl ether also known as butyl carbitol ((CH$_3$(CH$_2$)$_3$OCH$_2$- CH$_2$OCH$_2$CH$_2$OH, ACROS ORGANICS) and H$_2$O were used as solvents. These salts were mixed in different proportions as listed in Table 3.1. In this table, solution names coded as ratio of cobalt to iron and ethanol, H$_2$O and butyl carbitol, respectively. Total salt concentration was 0.02 mol/L. Solution names are given by using the first digits of their cobalt and iron percentages as well as their ethanol, water and butyl carbitol contents.

Table 3.1. Proportion of salts and solvent for all solutions. Amounts of lanthanum nitrate and strontium chloride were constant.

Solution Name	Cobalt	Iron	Ethanol	H$_2$O	Butyl carbitol	Conductivity (mS/cm)
82-820	80	20	80	20	0	1.085
28-820	20	80	80.0	20	0	1.749
82-306	80	20	33.3	0	66.7	0.041
28-306	20	80	33.3	0	66.7	0.050

3.2.3. Experimental Setup

All LSCF films were deposited using a vertical electrostatic spray deposition (ESD) system located in LEPMI, Grenoble, France. Installation is vertical to avoid the drops and any flow of the precursors solution on the substrate. The experimental setup is used for depositing of the coating is shown in Figures 3.4 and 3.5.

Figure 3.4. Schematic drawing of the ESD setup used in sample preparation

ESD process consists of:

  i. Electrostatic spray unit

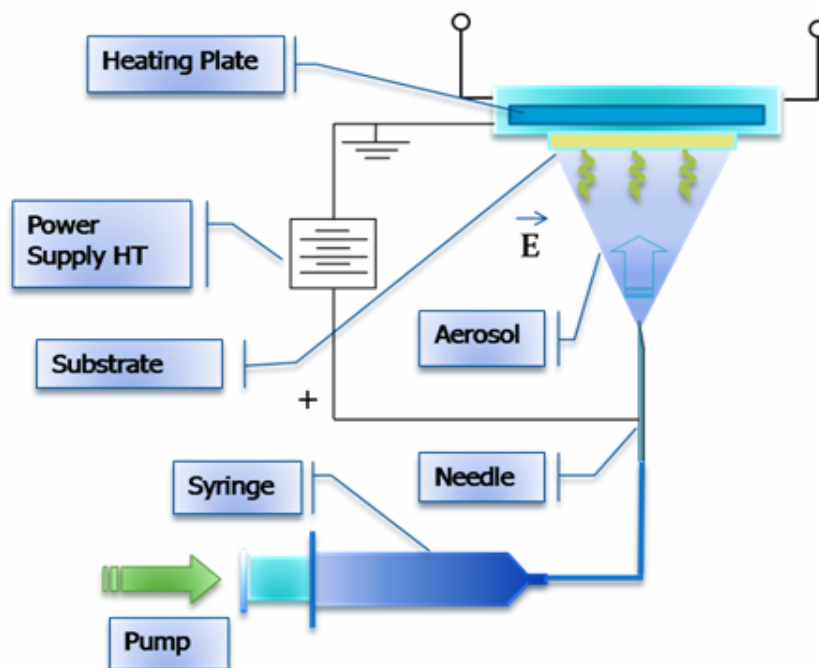 ii. A liquid precursor feed unit

  iii. Temperature control unit

The electrostatic spray unit comprises a high voltage power supply, a stainless steel nozzle and a grounded substrate holder. The liquid-precursor feed unit consists of syringe and a syringe pump (Kd Scientific M361). The temperature control unit for the deposition temperature includes a heating plate and a temperature controller connected to a thermocouple. Figure 3.5 shows a photograph of the entire setup.

When a sample was ready to be deposited, it was placed on the stainless steel holder with a 8 mm hole in the middle to allow sprayed material to coat a small area on the surface of the ceramic. Top side of the ceramic rested against a heating plate. The precursor solution was filled inside a 10 ml syringe (Becton Dickinson) which could be pushed at a controlled speed to deliver the desired amount of solution through the nozzle. A positive high voltage was applied to the stainless steel nozzle while the solution was sprayed. This high voltage produced electrostatically stressed, positively charged conically shaped droplets also known as Taylor cone (Chen, 1998) that were generated and directed to the grounded substrate. Eventually, the surface of the electrolyte ceramic was coated with a thin layer of cathode material. Upon contact with the heated substrate the solvent in the solution rapidly evaporates and an LSCF film with desired stoichimetry forms.

Figure 3.5. The photograph of ESD setup used in sample preparation (in LEPMI, Grenoble, France)

The following ESD process deposition conditions were recorded:

i.   Nozzle to substrate distance

ii.   Precursor solution flow rate

iii. Deposition temperature

iv.   Heat treatment

3.2.4. Experimental Plan

Experimental conditions for all samples were listed in Table 3.2. As shown in Figure 3.2, two separate ceramic substrates of CGO and TZ-3Y were used. The ceramic substrates coded C and Z, respectively. These were dense ceramics that were previously fired to achieve a low porosity substrate before being polished with diamond suspension. Polished samples were coated by an LSCF layer by ESD process. Final stage of processing was post heat treatment of the coated ceramics to achieve a mature ceramic coating.

(a)   (b)
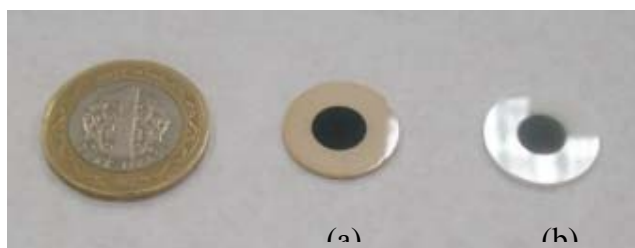
Figure 3.6. Samples after coating and sintering: (a) CGO sample, (b) TZ-3Y sample

3.3. Characterization

In this part, characterization techniques for investigating the $La_{0.6}Sr_{0.4}Co_{0.8}Fe_{0.2}O_{3-\delta}$, $La_{0.6}Sr_{0.4}Co_{0.2}Fe_{0.8}O_{3-\delta}$ were described. Characterization has a crucial role in interpreting the structure and property relationship between $La_{0.6}Sr_{0.4}Co_{0.8}Fe_{0.2}O_{3-\delta}$ and $La_{0.6}Sr_{0.4}Co_{0.2}Fe_{0.8}O_{3-\delta}$ on CGO and TZ-3Y. The techniques used were X-ray diffraction (XRD, Panalytical Xpert Pro MPD) and scanning electron microscopy (SEM, LEO Stereoscan S440) for microstructural characterization, thermogravimetric analysis (DTA/TG, Netzsch STA 409) for thermal property characterization.

3.3.1. Electrical Conductivity

The electrical conductivity of the precursor solutions was measured using a Tacussel CDRV 62 conductometer.

3.3.2. Differential Thermal Analysis (DTA/ TGA)

In order to determine the thermal decomposition temperatures, thermogravimetric analysis (TGA) was performed on $La_{0.6}Sr_{0.4}Co_{0.8}Fe_{0.2}O_{3-\delta}$, $La_{0.6}Sr_{0.4}Co_{0.2}Fe_{0.8}O_{3-\delta}$ solutions with DTA/TGA (Netzsch STA 409) under ambient atmosphere. Solutions of 100-130 mg were heated from room temperature to 690 °C at a heating rate of 10 °C/min.

3.3.3. Scanning Electron Microscopy

Scanning electron microscope (SEM, LEO Stereoscan S440) was used to investigate the surfaces of LSCF films and for interpreting the porous and dense microstructures.

3.3.4. X-Ray Diffraction Analysis

X-ray diffraction analysis (XRD) was performed using a PANalytical X'Pert Pro MPD diffractometer in the Bragg–Brentano geometry from 10 ° to 120 °, step size and step time were 0.017 ° and 241.3 sec, respectively.

Table 3.2. Experimental conditions for all the samples that were studied in this thesis

Sample Code No.	LSCF composition*	Distance (mm)	Flow rate (ml/h)	Deposition Time (h)	Deposition Temperature (°C)	Annealing Temperature (°C)	Solution Name
C1	6482	15	0.3	1	250	900	82-820
C2	6482	30	0.3	1	250	900	82-820
C3	6482	45	0.3	1	250	900	82-820
C4	6482	15	0.7	1	250	900	82-820
C5	6482	30	0.7	1	250	900	82-820
C6	6482	45	0.7	1	250	900	82-820
C7	6482	15	1.5	1	250	900	82-820
C8	6482	30	1.5	1	250	900	82-820
C9	6482	45	1.5	1	250	900	82-820
C10	6482	35	1.0	1	300	900	82-820
C11	6482	35	1.0	1	350	900	82-820
C12	6482	35	1.0	1	375	900	82-820
C13	6482	35	1.0	5	350	900	82-306
C14	6482	35	1.0	5	350	1100	82-306
C15	6482	35	1.0	5	350	1300	82-306
C16	6428	35	1.0	5	350	900	28-306
C17	6428	35	1.0	5	350	1100	28-306
C18	6428	35	1.0	5	350	1300	28-306
Z1	6482	35	1.0	5	350	900	82-306
Z2	6482	35	1.0	5	350	1100	82-306
Z3	6482	35	1.0	5	350	1300	82-306
Z4	6428	35	1.0	5	350	900	28-306
Z5	6428	35	1.0	5	350	1100	28-306
Z6	6428	35	1.0	5	350	1300	28-306
RC4	6428	15	0.7	1	250	900	28-306

* Subscripts designate compositions. For example 6482 = $La_{0.6}Sr_{0.4}Co_{0.8}Fe_{0.2}O_{3-\delta}$ and 6428 = $La_{0.6}Sr_{0.4}Co_{0.2}Fe_{0.8}O_{3-\delta}$

CHAPTER 4

RESULTS AND DISCUSSION

In this study, the results of experiments aimed at depositing $La_{0.6}Sr_{0.4}Co_{0.8}Fe_{0.2}O_{3-\delta}$, $La_{0.6}Sr_{0.4}Co_{0.2}Fe_{0.8}O_{3-\delta}$ films on CGO and TZ-3Y substrates were presented. In order to understand the process mechanisms and to interprete structural characterizations, the effect of nozzle to substrate distance, precursor solution flow rate, deposition temperature and applied voltage were tested. Also, electrical conductivity measurements of $La_{0.6}Sr_{0.4}Co_{0.8}Fe_{0.2}O_{3-\delta}$, $La_{0.6}Sr_{0.4}Co_{0.2}Fe_{0.8}O_{3-\delta}$ precursor solutions were made to understand the degree of dissolution of the components. Moreover, thermal analysis of the precursor solutions are presented in this chapter.

In order to see the effect of calcination treatment on the CGO powder samples were heat treated at 700 °C for 7 h in a laboratory box furnace (Carbolite Furnace HTC 1000). XRD analysis of the CGO powder before and after calcination were presented in Figure 4.1. No change in the phases present was observed (Figure 4.1).
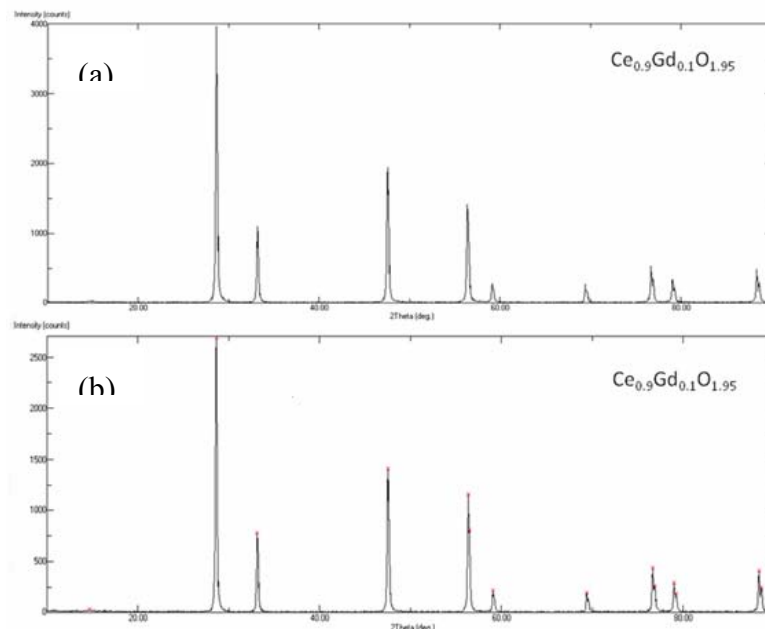

Figure 4.1. XRD diagrams of $Ce_{0.9}Gd_{0.1}Oxide$ powder (a) before and (b) after calcination at 700 °C 7 h

4.1. Electrical Conductivity Measurements

Electrical conductivities of all precursor solutions were measured using a Tacussel CDRV 62 conductometer at 18 °C. KCl salt solution with 0.1 M concentration was tested before these solutions were measured. The purpose was to calibrate the instrument. The measurements are listed in Table 4.1 where conductivities of all solutions were satisfactorily high indicating that they can be used in the ESD (Electostatic Spray Deposition) process.

Table 4.1. Conductivity values of all precursor solutions

Solution Name	Conductivity (mS/cm)
82-820	1.085
28-820	1.749
82-306	0.041
28-306	0.050

To associate with films morphology and conductivity of solutions, Ganan Calvo's relation can be used, because according to this relation as the electrical conductivity of the solution is increased, droplet size decreases (Neagu et al., 2006).

$$d \approx \sqrt[3]{\frac{\gamma \cdot \epsilon_0^2}{\sigma^2 \cdot \rho}} \tag{4.1}$$

According to Equation 4.1, d is the droplet size, γ is the surface tension, ϵ_0 is the electrical permittivity, ρ is the density and σ is the conductivity of the solution. In Table 4.1, first two solution and the other two solutions are considered with themselves because ethanol and water are used for first two solutions while ethanol and butyl carbitol are used for the others. According to C. Chen (1998), the lower limit of the conductivity varies between 10^{-8} and 10^{-11} S/m, while the upper limit can be to 10^{-1} S/m. The electrical conductivity values of pure ethanol, butyl carbitol are 60×10^{-6} and 0.2×10^{-6} S/cm (Lintanf et al., 2008) and water is 1×10^{-7} S/cm, respectively (Knovel 2008). As can be seen, these values of electrical conductivity of ethanol are higher than the butyl carbitol and water. In literature, typically, droplet size ranges from 2 to 10 μm (Neagu et al., 2005).

4.2. Differential Thermal Analysis (DTA/ TGA)

Generally, instead of one solvent a mixture of two or more solvents is more appropriate due to increased solubility of the salts and better control of the evaporation over a larger temperature interval along with reduced risk of cracking of the coating (Neagu et al., 2005).

Two types of LSCF solutions with $La_{0.6}Sr_{0.4}Co_{0.8}Fe_{0.2}O_{3-\delta}$ and $La_{0.6}Sr_{0.4}Co_{0.2}Fe_{0.8}O_{3-\delta}$, stoichiometry were prepared by dissolving their precursor salts in three different solvents (water, ethanol and butyl carbitol). In Figure 4.2, the three different solvent mixture compositions are marked on a triangular plot to show the ratio of ethanol, butyl carbitol and water.
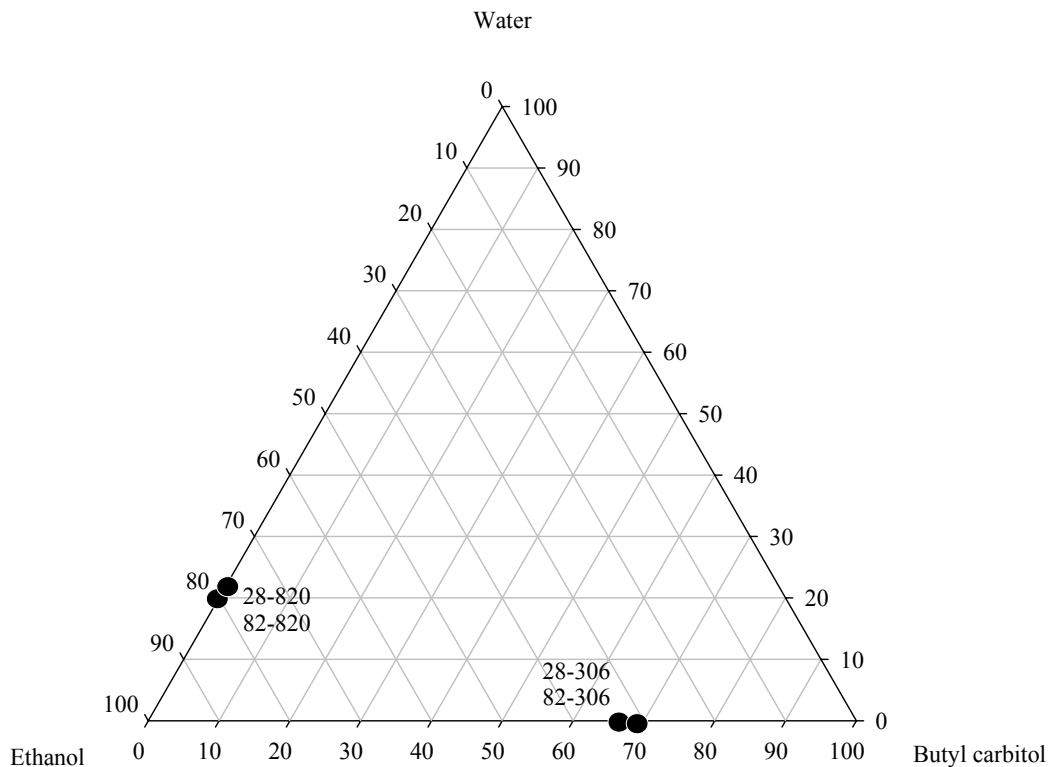

Figure 4.2. The mixtures prepared from three solvents.

DTA/TGA analyses were performed on all of the solutions mentioned to study their thermal behavior. The temperature range for the measurements ranged from room temperature to 690 ℃ at 10 ℃/min in air. The resulting graphs are shown in Figures 4.2 to 4.5.

In Figure 4.3, an endothermic peak at 118 °C was observed due to the evaporation of the solvent for the 82-820 and 28-820 samples. The evaporation

temperature of H_2O is 100 °C while that of ethanol is 78 °C. TGA analyses results in Figure 4.4 also confirmed the DTA observations.
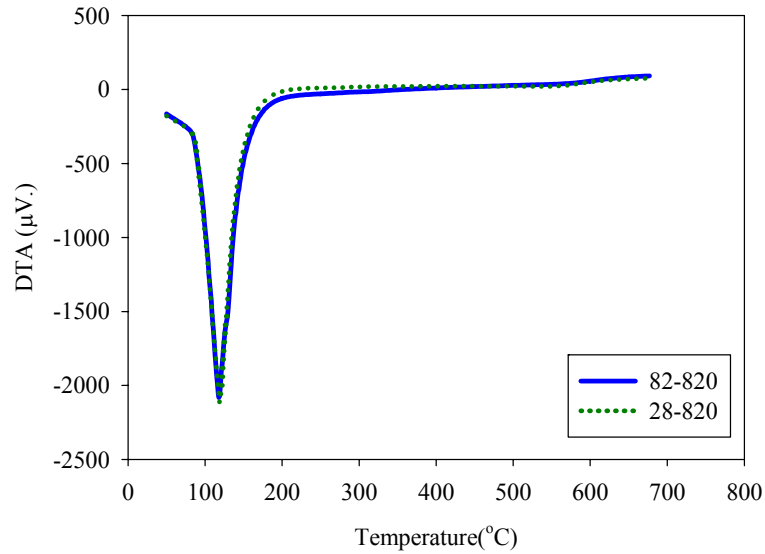

Figure 4.3. DTA analyses of 82-820 and 28-820 solutions performed under atmospheric conditions at a heating rate of 10 °C/min.

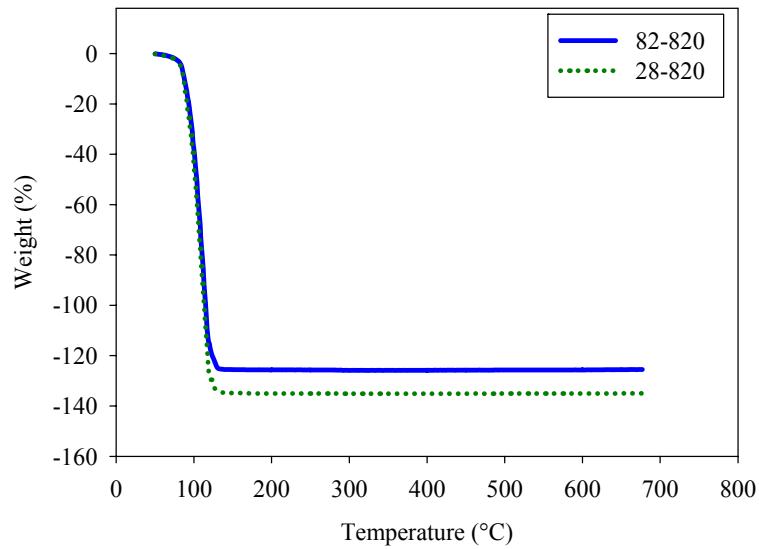Figure 4.4. TGA analyses of 82-820 and 28-820 solutions performed under atmospheric conditions at a heating rate of 10 °C/min.

In Figure 4.5, DTA analyses results for solutions with mixtures of ethanol and butyl carbitol (also see Figure 4.1) are presented. There were two main endothermic peaks at 136 °C and 245 °C corresponding to the evaporation of ethanol and butyl carbitol, respectively. The former evaporated at a range of temperatures of 95 °C to 210 °C while the evaporation temperature range for butyl carbitol was narrower. A narrow evaporation temperature range may be helpful for formation of solid crust on ceramic

electrolyte. Weight loss as a function of temperature graph (TGA chart in Figure 4.6) of the solutions further confirmed the DTA observations that butyl carbitol evaporates faster and at higher temperature.
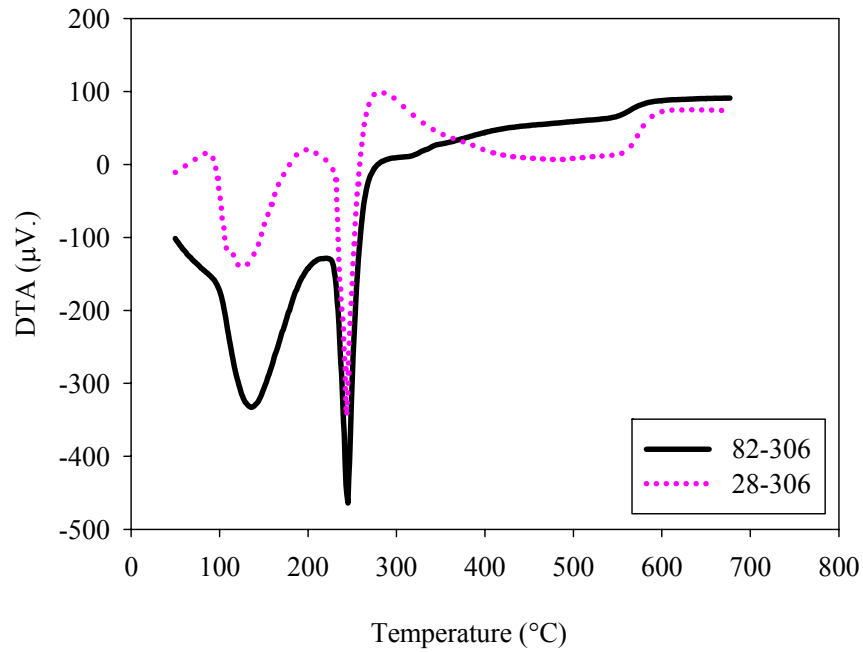

Figure 4.5. DTA analyses of 82-306 and 28-306 solutions performed under atmospheric conditions at a heating rate of 10 °C/min.
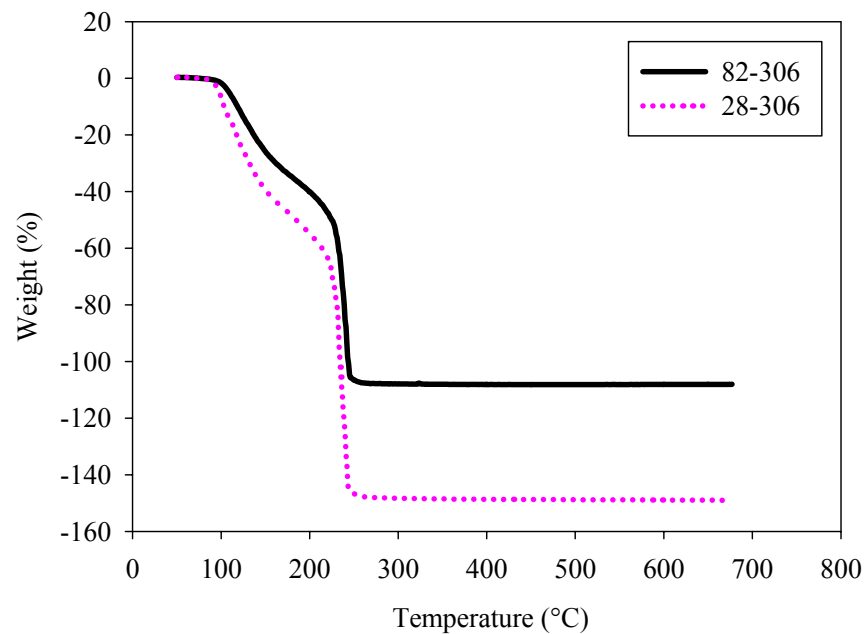

Figure 4.6. TGA analyses of 82-306 and 28-306 solutions performed under atmospheric conditions at a heating rate of 10 °C/min.

4.3. Electrostatic Spray Deposition (ESD)

The ceramic electrolyte samples were coated with LSCF films using the ESD apparatus as explained in section 3.2.3. A set of experiments were conducted at 5-15 kV of voltage, 0.3-1.5 ml/hour of solution flow rate, 250-375 °C of heating temperature of the electrolyte and 15-45 mm of nozzle to substrate distance. Coating process was successfully performed without any peeling from the surface.

4.4. Post Heat Treatment

After the ceramic electrolyte samples were coated with LSCF films they were heat treated at 900°C for 2 hours in a laboratory furnace to form the well- developed cathode layer.

4.5. Scanning Electron Microscopy

After the ceramic electrolyte substrates were coated and annealed, their structures were investigated by using Scanning Electron Microscope. Two separate studies were made. First, coating surfaces and next the fracture surfaces were observed at high magnification.

To understand the influence of annealing on film morphology, first the CGO substrate was deposited using a flow rate of 1.0 ml/h, nozzle to substrate distance of 35mm and substrate temperature of 375 °C for 2 h. Then, this sample was annealed at 900 °C for 2 h. The resulting structure of the coating before and after annealing was compared to find out if film densification increased after annealing because of evaporation of organic residues. The difference of the micrographs can be seen in Figure 4.7. SEM micrographs taken before and after annealing show that heat treatment in air at 900 °C for 2 h. A slight decrease in film thickness due to the film densification and departure of organic residues (Marinha et al., 2009). All remaining samples in this thesis were observed after annealing at 900 °C for 2 h.
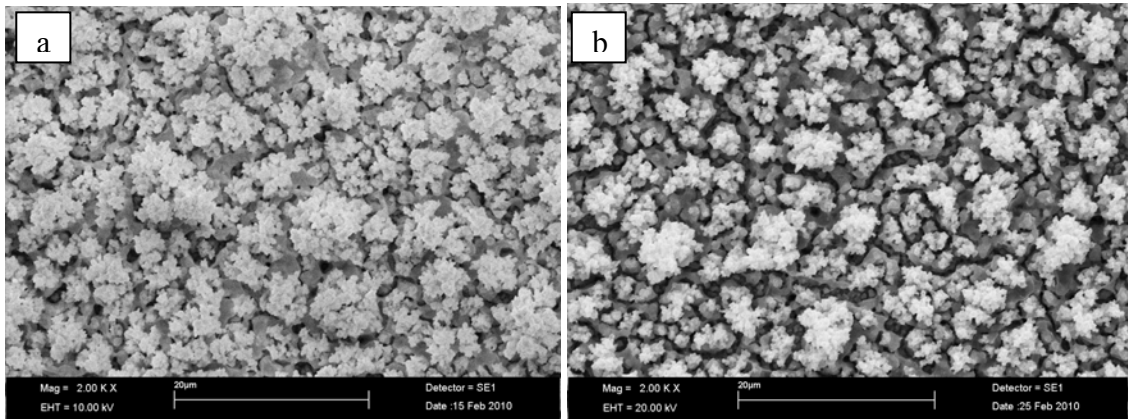
Figure 4.7. SEM micrographs of the surface of the film, (a) before and (b) after annealing at 900 °C for 2 h and applied voltage is 14 kV

LSCF films are observed to investigate the effects of some deposition parameters on the surface morphology of thin films. Properties of LSCF deposits can be modified by changing the following parameters:

I.   nozzle to substrate distances
II. solution flow rates
III. deposition temperatures
IV. heat treatment.

Applied voltage was varied within a narrow margin of 5-15 kV in all experiments. Its effect is expected to be insignificant under the conditions studied in this thesis.

4.5.1. Influence of Nozzle to Substrate Distance

To study the effect of spraying distance on the morphology of the LSCF films, depositions were carried out at nozzle to substrate distances of 15 mm, 30 mm and 45 mm and flow rates ranged from 0.3 ml/h, 0.7 ml/h and 1.5 ml/h for 1 h at 250 °C as shown in Figure 4.8. According to the first column (C1, C2 and C3), second column (C4, C5 and C6) or third column (C7, C8 and C9), when the distance increases, droplets will be smaller and drier and a very dense microstructure can be obtained, because higher distance will dry up the droplets. It means that, as nozzle to substrate distance increases, deposited particles become increasingly smaller due to larger solvent losses through evaporation occurring during droplet flight. A minor amount of

evaporative cooling between the nozzle and the substrate can be expected (Marinha et al., 2009).
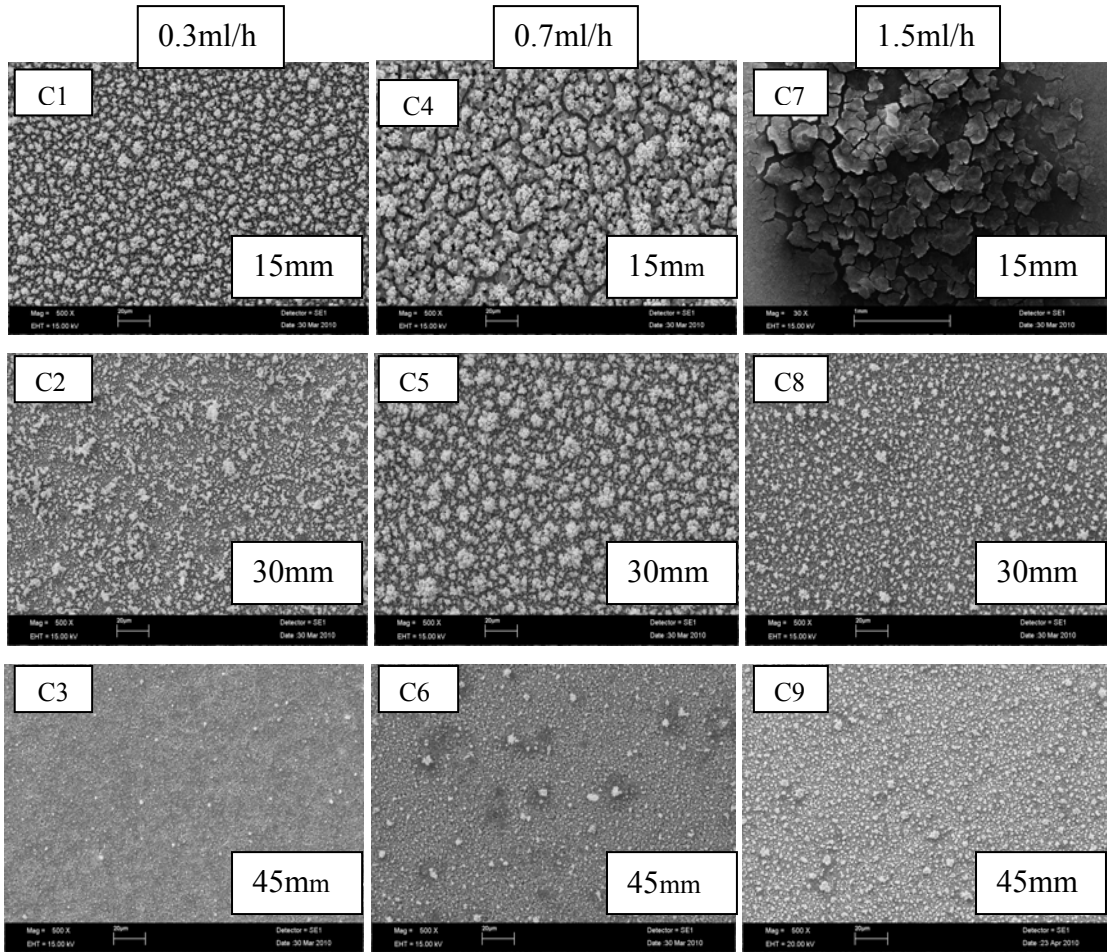

Figure 4.8. SEM micrographs of $La_{0.6}Sr_{0.4}Co_{0.8}Fe_{0.2}O_{3-\delta}$ films deposited on CGO substrate using three different flow rates of 0.3 ml/h, 0.7 ml/h and 1.5 ml/h for 1 h and at a constant temperature 250 °C for three different nozzle to substrate distances of 15 mm (first line), 30 mm (second line) and 45 mm (last line). Applied voltage was kept constant at 14 kV

The proportions of the elements displayed by EDS results helped to be sure to identify $La_{0.6}Sr_{0.4}Co_{0.8}Fe_{0.2}O_{3-\delta}$ and $La_{0.6}Sr_{0.4}Co_{0.2}Fe_{0.8}O_{3-\delta}$ films on the CGO and TZ-3Y substrates (Figures 4.9 and 4.10, Tables 4.2, 4.3). The observed compositions of prepared films are also shown to be in moderately good agreement with the starting solutions. Some Ce and Gd also showed up in EDS measurements but these are removed in this table to facilitate better comparison with theoretical data in Tables 4.2 and 4.3.
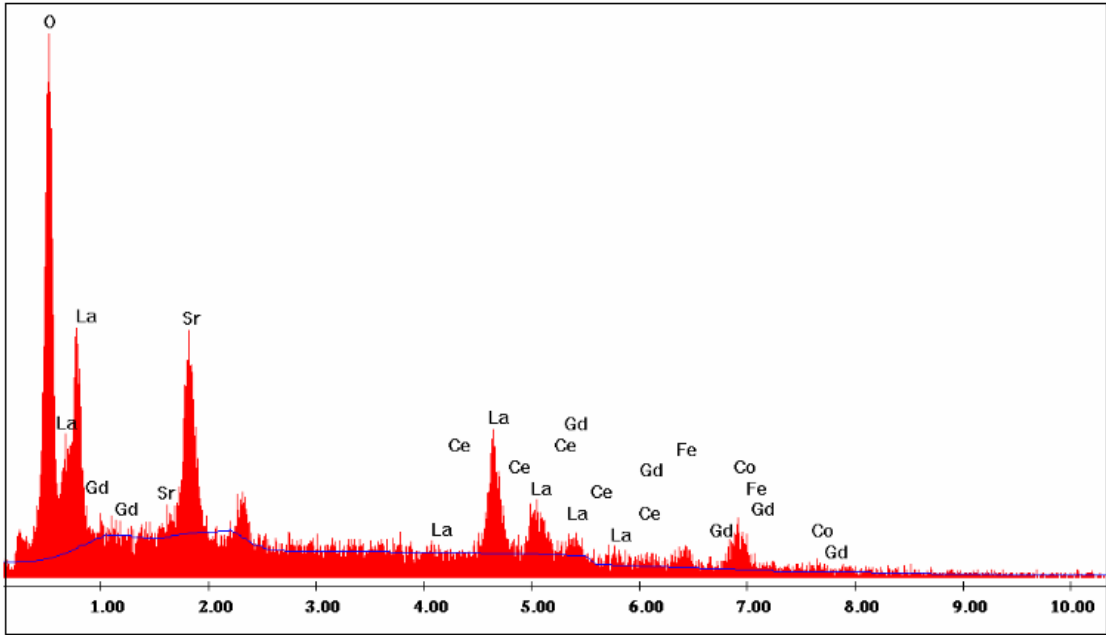
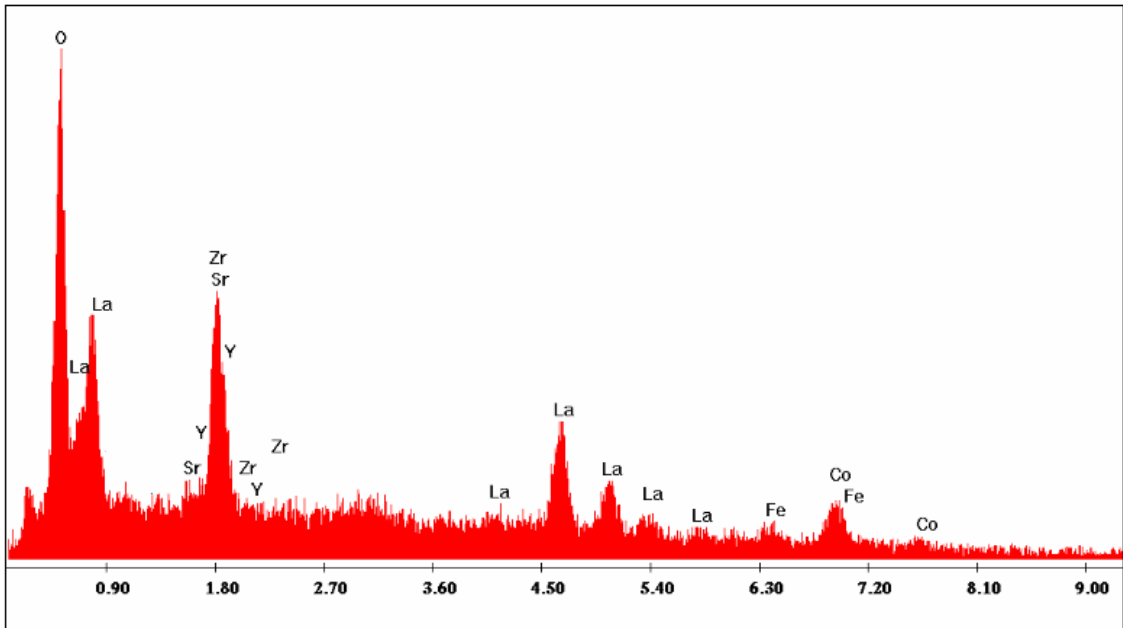Figure 4.9. EDS analysis of $La_{0.6}Sr_{0.4}Co_{0.8}Fe_{0.2}O_{3-\delta}$ on CGO substrate

Figure 4.10. EDS analysis of $La_{0.6}Sr_{0.4}Co_{0.8}Fe_{0.2}O_{3-\delta}$ on TZ-3Y substrate

Table 4.2. EDS analysis results of chemical compositions of $La_{0.6}Sr_{0.4}Co_{0.8}Fe_{0.2}O_{3-\delta}$ films

Element (wt%)	EDS analysis wt%	
	Theoretical	Measured
La	37.0	41.9
Sr	15.6	14.2
Co	20.9	24.3
Fe	5.0	6.5
O	Balance	Balance

Table 4.3. EDS analysis results of chemical compositions of $La_{0.6}Sr_{0.4}Co_{0.2}Fe_{0.8}O_{3-\delta}$ films

Element (wt%)	EDS analysis wt%	
	Theoretical	Measured
La	37.4	43.0
Sr	15.7	13.5
Co	5.3	9.2
Fe	20.0	20.5
O	Balance	Balance

4.5.2. Influence of Precursor Solution Flow Rate

When influence of the flow rate is analyzed, higher flow rate will produce larger droplets which are more difficult to dry upon flight, because when the solution flow rate is increased, larger droplets are accumulated and dispatched from the nozzle. Large sized droplets contain more liquid which can take longer flight distances without complete drying. This can be confirmed by comparing the morphology of the films deposited at different flow rates. Microstructures of films deposited using solution flow rates that were varied from 0.3 to 1.5 ml/h are shown in Figures 4.8 C1-C7, C2-C8 or C3-C9. All photographs in Figure 4.8, except C7, indicated an improved reticulated structure upon increased solution flow rates. Sample C7 did not coat well the surface of the substrate because of its excessively high liquid content (Figure 4.11). As shown in Figure 4.9, at short distances, many cracks are present at high flow rate because the droplets include larger amounts of solvent which can not find sufficient time to evaporate during their flight.
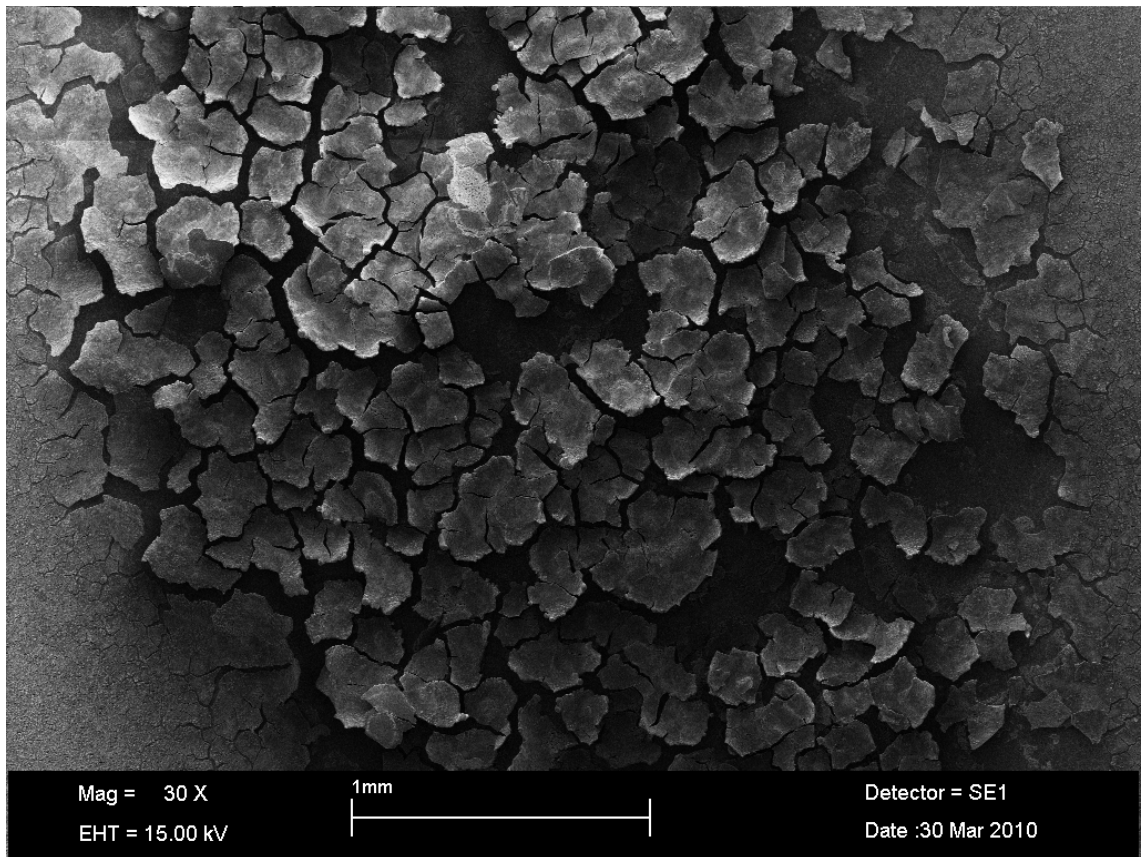
Figure 4.11. SEM image of the surface of C7 sample of $La_{0.6}Sr_{0.4}Co_{0.8}Fe_{0.2}O_{3-\delta}$ layer deposited on a CGO substrate at 0.7 ml/h from a nozzle to substrate distance of 15 mm for 1 h at 250 °C and applied voltage is 14 kV

When the samples C3, C6 and C9 are broken and observed from their profiles, the effect of flow rate can be better understood (Figures 4.12 a to c). As mentioned before, as the flow rate of precursor solution increased, sprayed droplets increased in size and also increase of layer thickness can be seen, clearly. It is not possible in order to determine microstructure which obtain dense or porous by looking at the microstructure of the flow rate because degree and type of reticulation microstructure depend on a combination of both distance and flow rate.
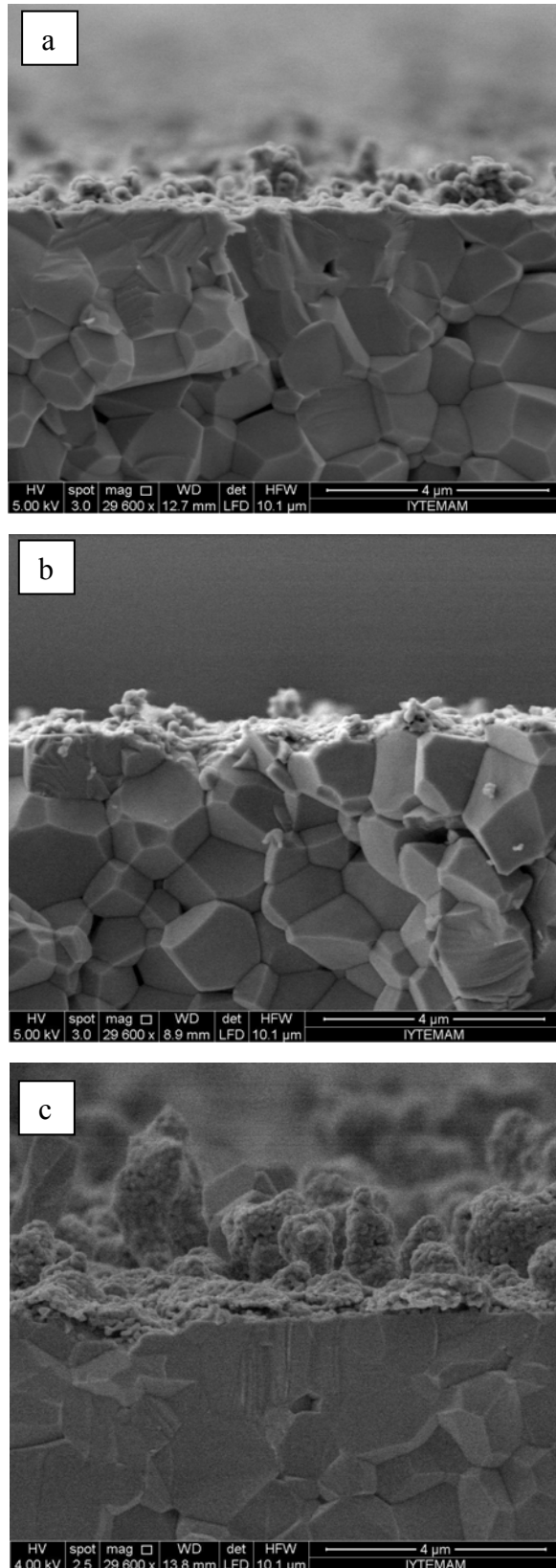
Figure 4.12. SEM images of the fracture surfaces of $La_{0.6}Sr_{0.4}Co_{0.8}Fe_{0.2}O_{3-\delta}$ films deposited on a CGO substrate at (a) 0.3 (b) 0.7 and (c) 1.5 ml/h from a nozzle to substrate distance of 45 mm for 1 h at 250 °C (samples C3, C6 and C9) by using 14 kV

4.5.3. Influence of Deposition Temperature

Deposition temperature (or the substrate temperature) has an important influence on the quality of coating because it affects the drying rate and the degree of spread of the droplets after impact with the substrate. It may even be speculated that the drying rate of the droplets during flight depends on the temperature of the substrate (Figure 4.13). Moreover, obtaining dense or porous microstructure correlates with spreading of the droplets on the surface.

In Figure 4.14, the effect of substrate temperature (300, 350 and 375 °C) on morphology of the deposited films was studied by keeping all other parameters constant. These specimens are coded C10, C11 and C12 which are listed in Table 3.2. As seen in Figure 4.14, at higher temperatures the droplets dried more and became smaller by producing a more dense structure.

Under the subject of effect of the temperature, preferential landing effect is another important point to mention, because this effect is a determining factor in order to decide if the temperature is too high or not (Marinha et al., 2009). In this thesis, the temperatures were convenient and preferential landing effect was not observed.
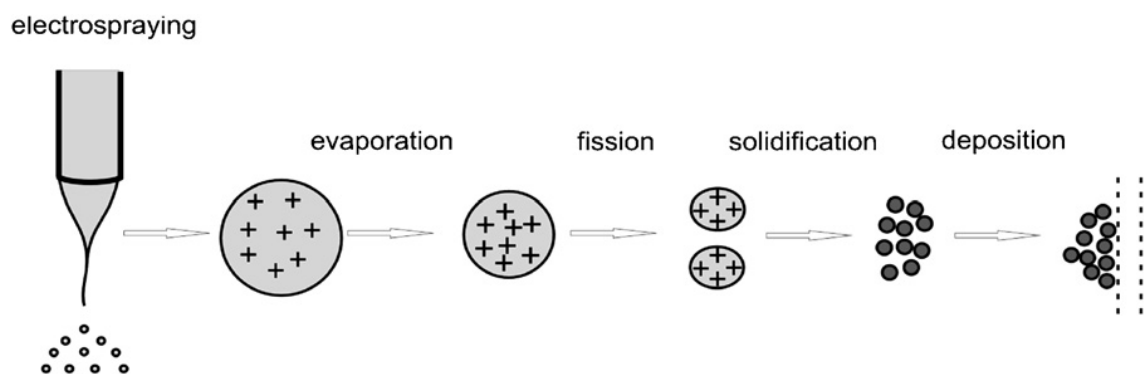

Figure 4.13. Steps of a particle production by electrospraying
(Source: Jaworek et al., 2008)

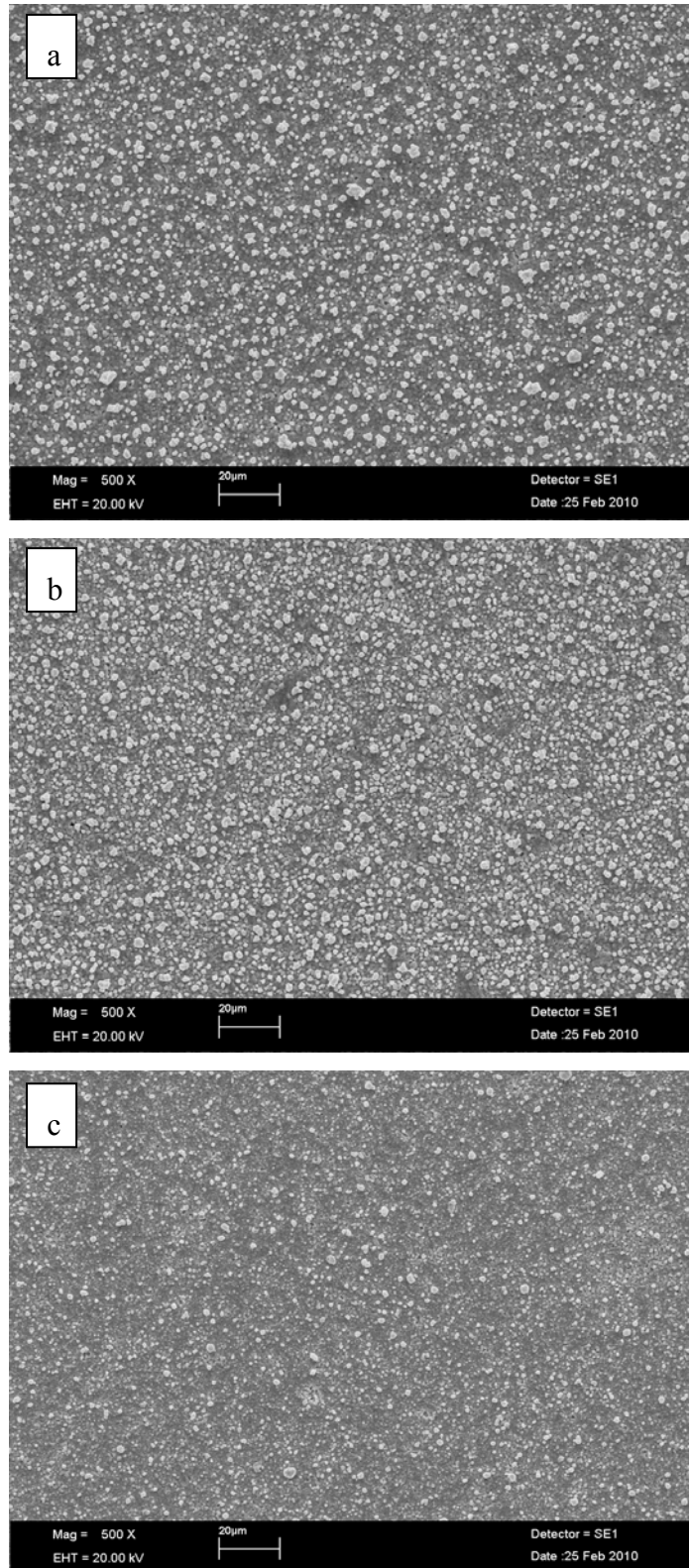Figure 4.14. SEM micrographs of $La_{0.6}Sr_{0.4}Co_{0.8}Fe_{0.2}O_{3-\delta}$ coated samples of CGO substrates using different temperatures (a) sample C10 at 300 °C, (b) sample C11 at 350 °C and (c) sample C12 at 375 °C. All runs were done at 14 kV

Keeping in mind that the LSCF films are covered on ceramic electrolyte substrates to serve as a cathode layer, the films must be continuous with good reticulated structure to provide the desired electrical conductivity. One may ask what is the best structure for good reticulation. Figure 4.15 shows a sample (RC4) with good reticulated structure that was obtained with a flow rate of 0.7 ml/h at 250 °C at a distance of 15 mm.
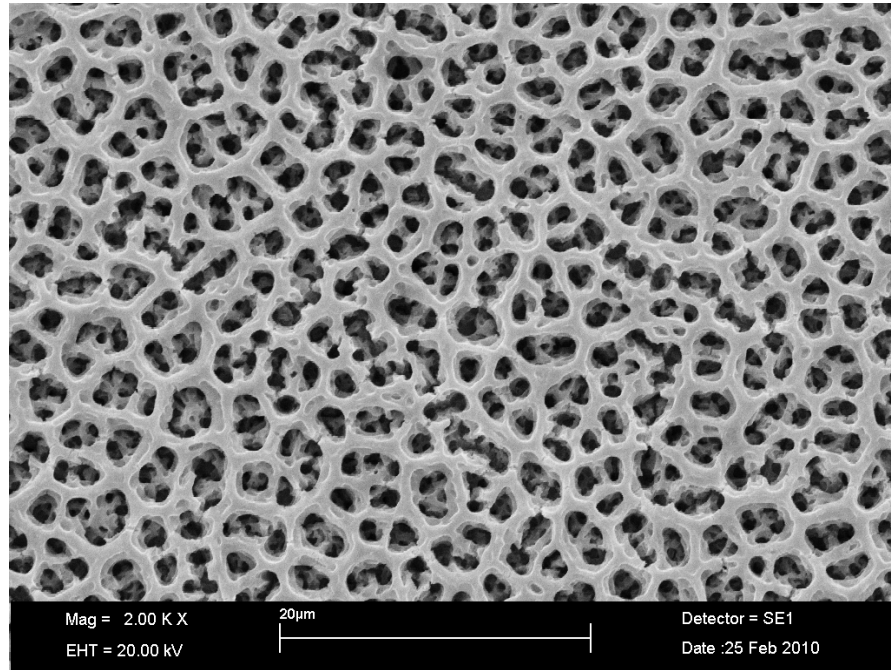

Figure 4.15. SEM micrographs of sample RC4 showing a well developed reticulated structure by applying 5 kV

4.5.4. Influence of Heat Treatment

In the light of the above mentioned information, in order to see the effect of post annealing heat treatment temperature on the CGO and TZ-3Y microstructures, C13, C14, C15, Z1, Z2 and Z3 tests were conducted by keeping all other experimental conditions constant. The results are shown in Figure 4.16. At 900 °C both CGO and TZ-3Y substrates showed similar microstructures. As the temperature was increased, grain size did not grow significantly, pores closed and surface area appeared to decrease. The coating showed a densified structure due to sintering as the temperature increased.
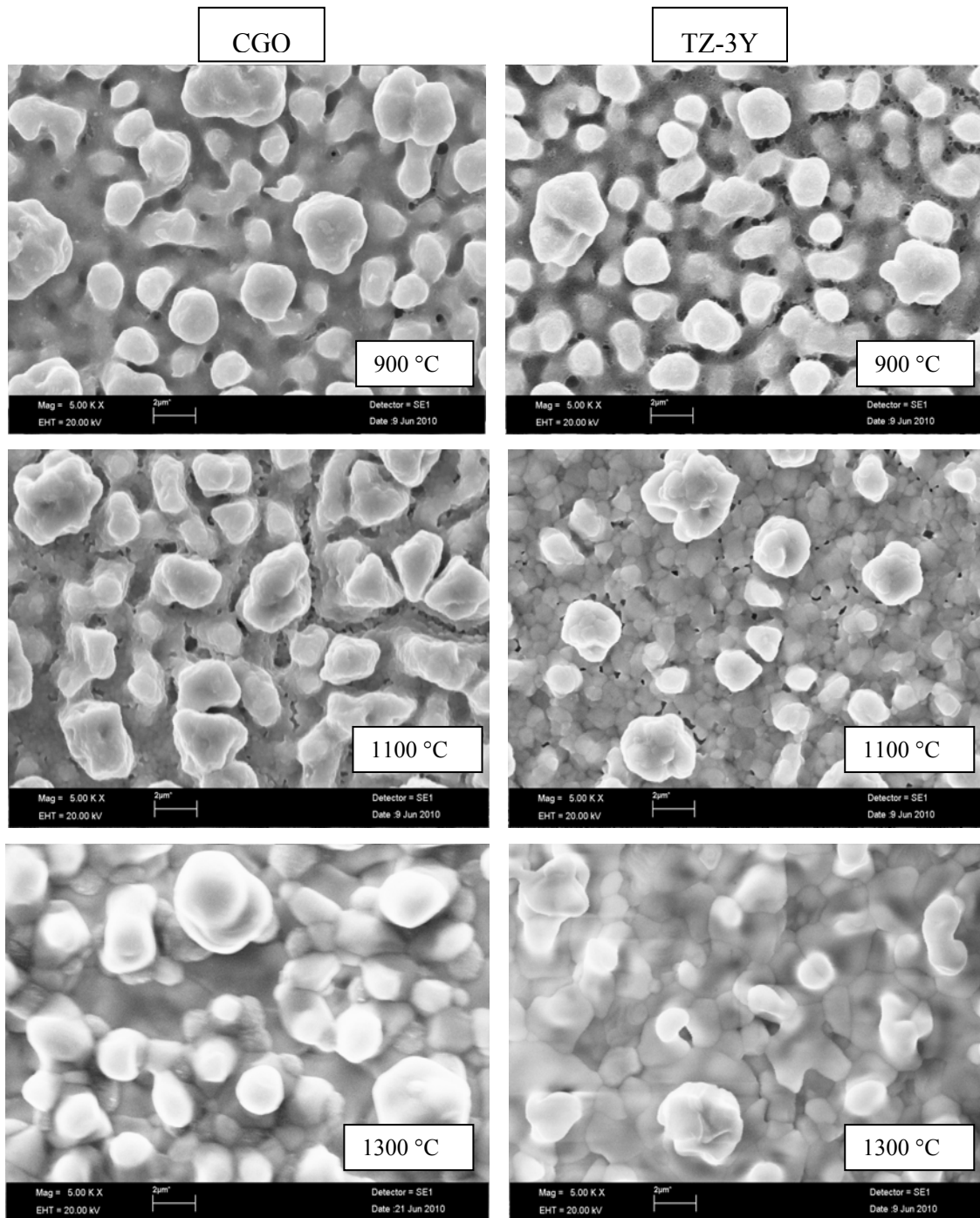
Figure 4.16. Influence of heat treatment temperature of La$_{0.6}$Sr$_{0.4}$Co$_{0.8}$Fe$_{0.2}$O$_{3-\delta}$ films on CGO (samples C13, C14 and C15 on left column) and TZ-3Y (samples Z1, Z2 and Z3 on right column) by applying 15 kV

To obtain more detailed information about the quality of coating and the degree of bonding in the samples C13 and Z1, their profile SEM pictures were taken from fracture surfaces of broken sample cross sections. These fracture surfaces are shown in Figures 4.17 and 4.18. A crack-free bond was found to form between the substrate and the coating. The coating was porous and continuous with a minimum thickness of

roughly 1 μm for both C13 and Z1 samples which were heat treated at 900 °C for 1 hour (Figure 4.16). C15 and Z3 samples that were heat treated at 1300 °C appeared to be highly dense and glassy and were free from pores (Figure 4.17).
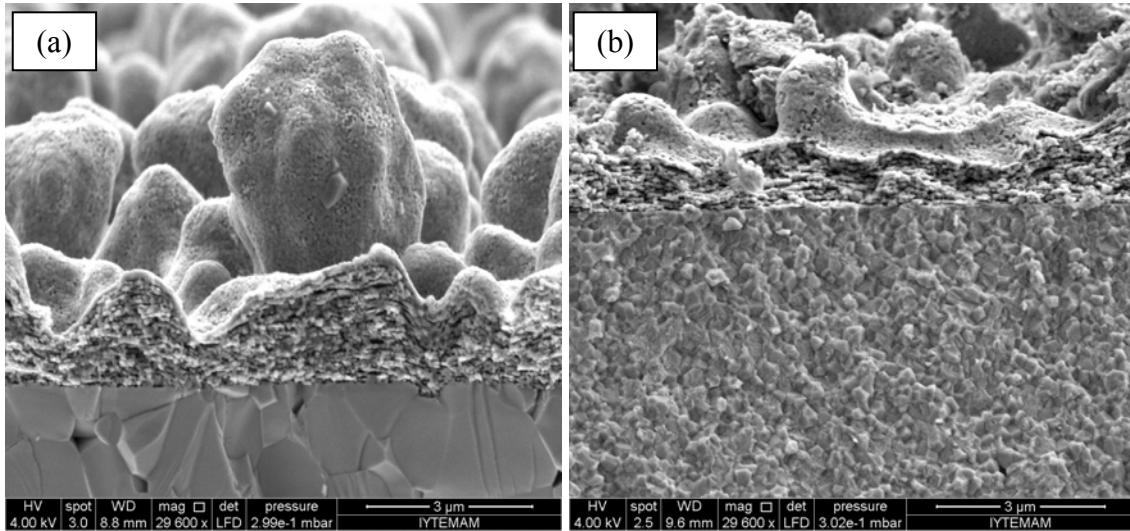

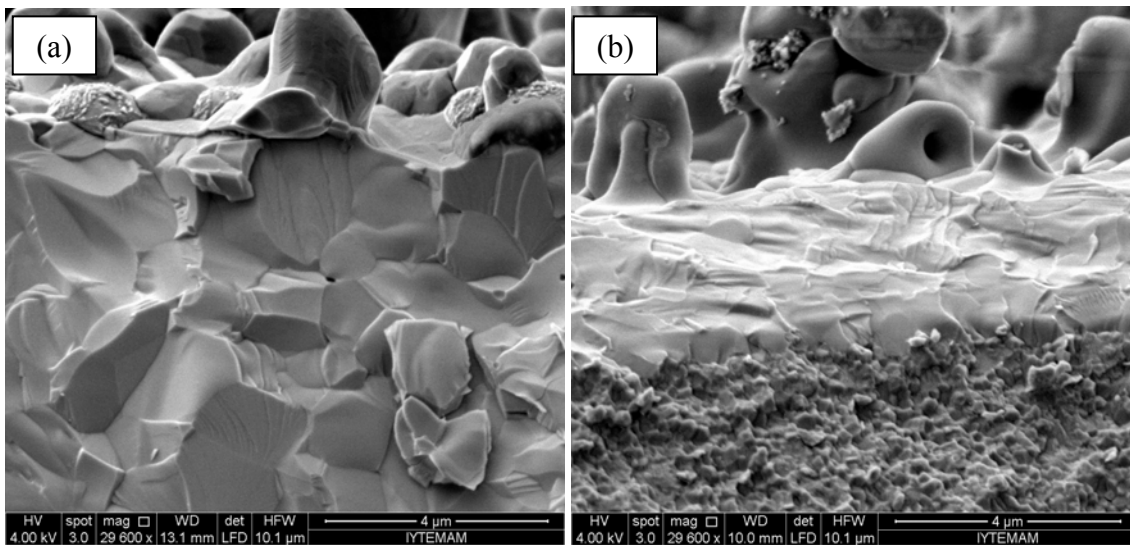Figure 4.17. Fracture surfaces of cross sections of (a) sample C13 and (b) sample Z1 coatings that were both annealed at 900 °C.

Figure 4.18. Fracture surfaces of cross sections of (a) sample C15 and (b) sample Z3 coatings that were both annealed at 1300 °C. Glassy structure of the coating is evident in both SEM photomicrographs.

Figure 4.19 shows that the ceramic substrate materials of CGO and TZ-3Y had different grain sizes. Average grain size of CGO sample is obviously larger than the TZ-3Y sample. Equation 4.2 were used to measure the average particle sizes of the ceramic substrates. In order to apply of equation 2.1, N1 refers to the number of the

total grains in the image, N2 refers to the half grains in the image, L is length of the image and h is height of the image (Emre Yalamaç 2010). Photographs in Figures 4.19 and 4.20 were used for this purpose. Average grain sizes of the CGO and TZ-3Y matrices heated at 900 and 1300 °C were found to be in the range of 1.75-183 μm and 0.35-0.40 μm, respectively.

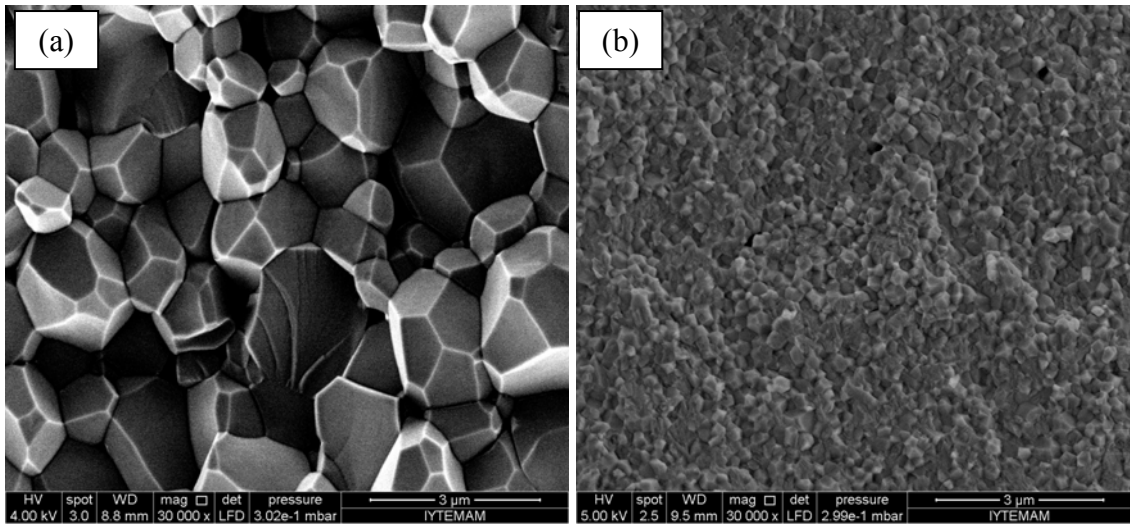$$\bar{D} = 1.38 * \sqrt{\frac{L*h}{(N1+\frac{N2}{2})}} \tag{4.2}$$

Figure 4.19. SEM micrographs of fracture surfaces of (a) CGO and (b) TZ-3Y substrates after coating and subsequent thermal treatment at 900 °C.
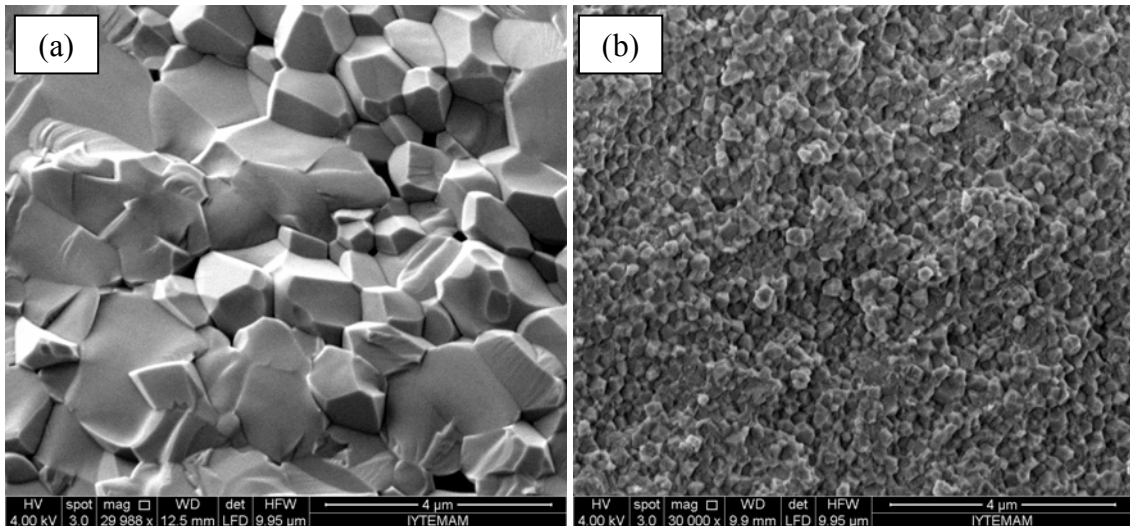

Figure 4.20. SEM micrographs of fracture surfaces of (a) CGO and (b) TZ-3Y substrates after coating and subsequent thermal treatment at 1300 °C.

4.6. X-Ray Diffraction Analysis

In this section, the results of X-ray diffraction (XRD) analyses are presented. X-ray diffraction analyses were performed to investigate if there is any change caused by the temperature. Figure 4.21 shows the XRD chart for sample C13 that was heat treated at 900 °C. Because the x-ray irradiated area on the specimen surface was larger than the area covered by LSCF coating some peaks from the substrate inevitably appeared on XRD analysis charts. CeO_2 (see also Table 4.4), for example, was observed in C13 sample as shown in Figure 4.21. It is actually the host crystal lattice of the $(Ce_{0.9}Gd_{0.1}O)$ CGO compound. Gadolinium is only 10 mol percent of CGO and forms the solute in the solid solution within CeO_2 lattice. Minor amount of La_2O_3 and LSCF-6491 $(La_{0.6}Sr_{0.4}Co_{0.9}Fe_{0.1}O_3)$ were also observed. But the observed compound was 6491. Therefore some deviation from expected compositions occurred.
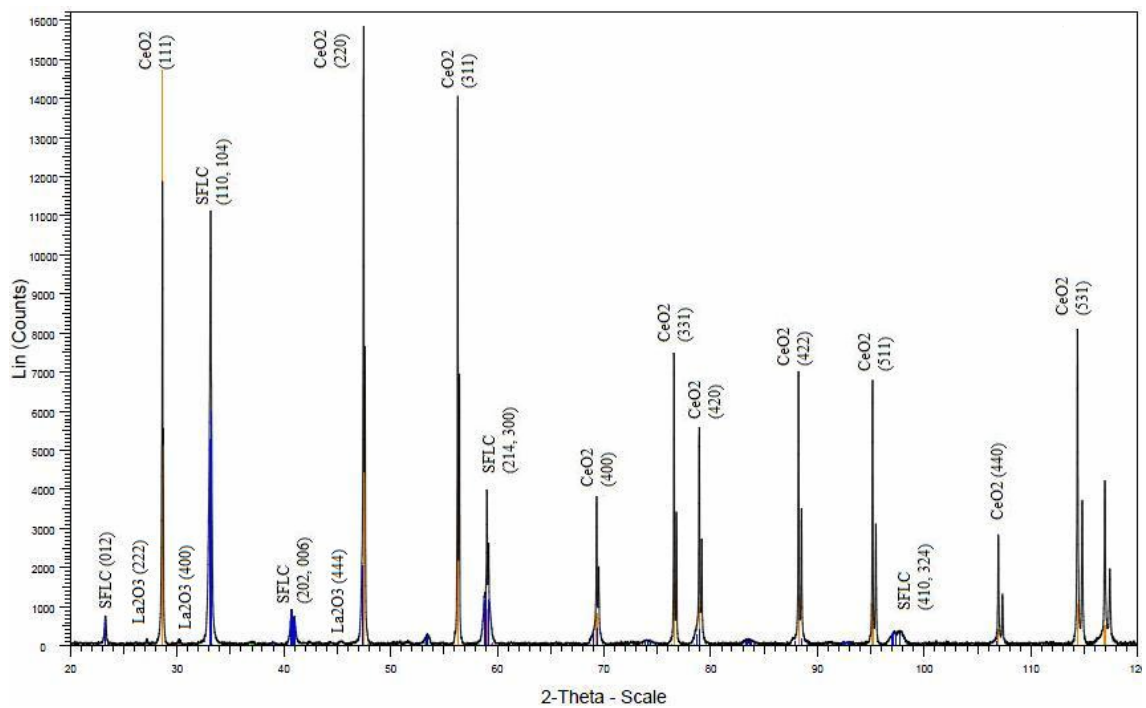

Figure 4.21 XRD chart for sample C13

Table 4.4. Phases observed in XRD analysis and their reference card numbers

Compound code used in XRD chart peak labels	Mineral composition	JCPDS reference number
LSCF-6491	$La_{0.6}Sr_{0.4}Co_{0.9}Fe_{0.1}O_3$	00-049-0283
CeO_2	CeO_2	34-0394
La_2O_3	La_2O_3	03-065-3185
LSCF-6482	$La_{0.6}Sr_{0.4}Co_{0.8}Fe_{0.2}O_3$	00-048-0124
ZrO_2	ZrO_2	50-1089
LSC	$La_{0.5}Sr_{0.5}(CoO_3)$	01-075-8571
SZO	$SrZrO_3$	04-001-7315
LZO	$La_2(Zr_2O_7)$	01-070-5602
LaO	LaO	04-007-4019
LSCF-7337	$La_{0.7}Sr_{0.3}Co_{0.3}Fe_{0.7}$	01-089-1268
SLF	$Sr_{0.6}La_{0.4}FeO_3$	04-007-6519
LSC	$La_{0.6}Sr_{0.4}(CoO_3)$	01-089-5717

In order to better understand the evolution of the phase composition in the coating samples of CGO were analysed by high temperature XRD (HTXRD) device in Lille University, France. In Figure 4.22, HTXRD analysis results for sample C13 is given. It should be noted that the post heat treatment was not applied. Peaks from the substrate are obviously observed to slightly shift left toward lower 2θ values. This was expected because of expansion of the lattice as a result of higher atomic vibrations at higher temperatures (Cullity 1974). Upon heating of the sample to 500°C and higher LSCF was observed to form on the coating. At 1100 °C the peaks for LSCF were stronger. In Figure 4.23, XRD analysis of the sample C15, which was heat treated at 1300 °C, is given. Peaks for LSCF-6482 were observed along with stronger peaks from the CeO_2 from the substrate (see Table 4.4 and Figure 4.23). The high temperature post heat treatment transformed some of the phases and produced a dense microsctructure as shown in Figure 4.17a. The XRD chart showed that the LSCF layer was not glassy but dense and crystalline.

Figure 4.24 shows the XRD analysis result for sample Z1, which was made to produce LSCF coating on TZ-3Y substrate. But the post heat treatment temperature was 900°C and some of the salts in the coating dissociated to produce an intermediate compound $La_{0.5}Sr_{0.5}(CoO_3)$. Apparently iron was not yet accommodated in the structure to enable formation of LSCF. When the same sample was heated to 1300°C after coating LSCF-7337 ($La_{0.7}Sr_{0.3}Co_{0.3}Fe_{0.7}$) as well as SZO ($SrZrO_3$), LZO ($La_2(Zr_2O_7)$) and LaO were observed in Figure 4.25. Notice that the LSCF was still not the intended 6482 composition but a La and Fe-rich phase formed instead. While there was no iron in Figure 4.24 in the LSC composition at 900°C heated sample, sample Z3 in Figure 4.26 was able to produce an Fe-rich LSCF compound. Sample Z1, for example, contained CeO_2 and LSC phases without much iron. When the same sample was heated to 1300 °C (sample Z3) iron took part in the reaction and LSCF was identified (Figure 4.25). Another significant observation from Figure 4.25 is that zirconia stole some of the La and Sr and therefore an LSCF compound with 7337 stoichiometry formed instead of the desired 6482 compound. The substrate CGO, on the other hand, was able to produce complete LSCF-6482 stoichiometry after 1300 °C heat treatment (sample C15). A lower temperature heat treatment was insufficient to achieve the desired stoichiometry (sample C13).
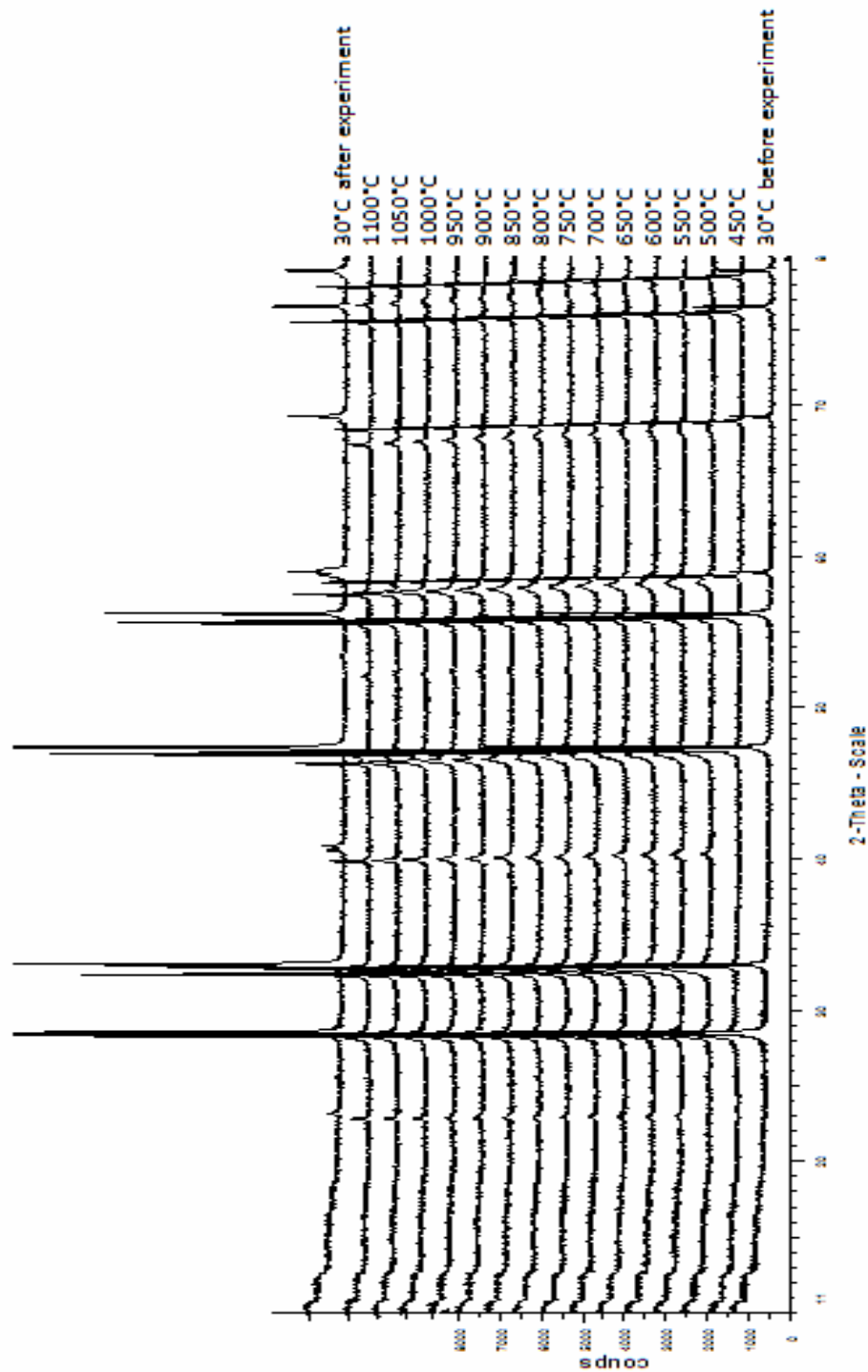
Figure 4.22. HTXRD result of La$_{0.6}$Sr$_{0.4}$Co$_{0.8}$Fe$_{0.2}$O$_{3-\delta}$ on CGO. This sample was prepared under the same conditions with C13 but without the post heat treatment
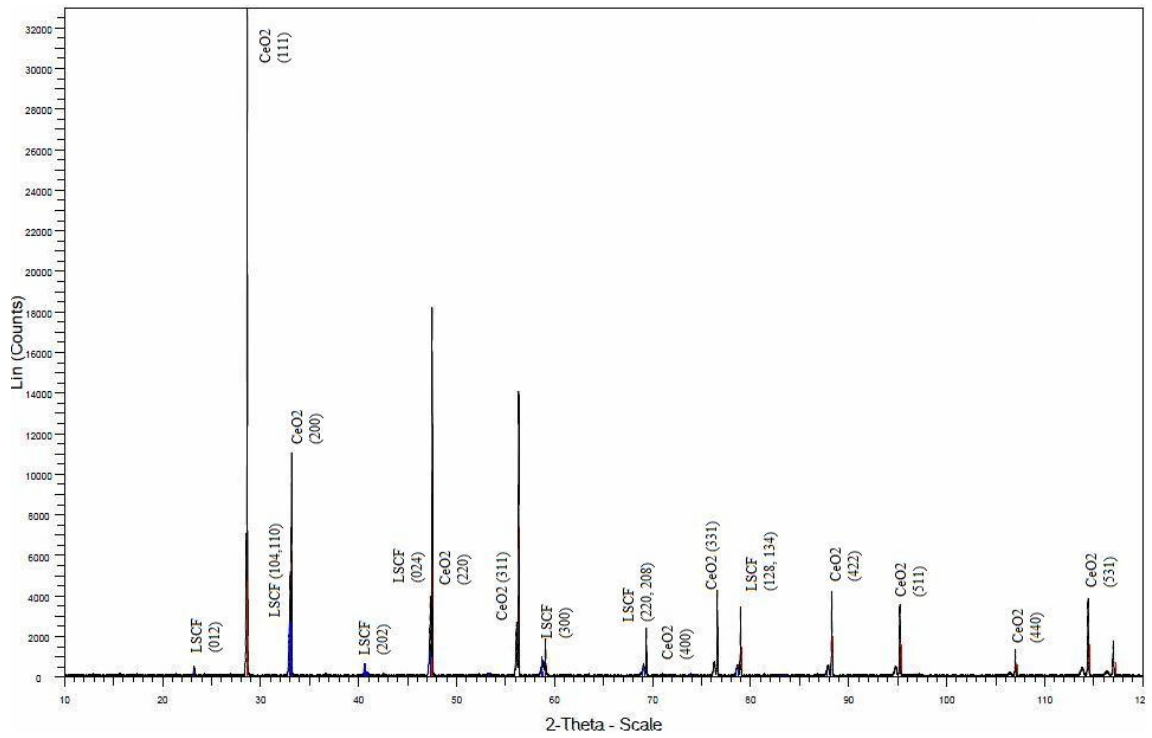
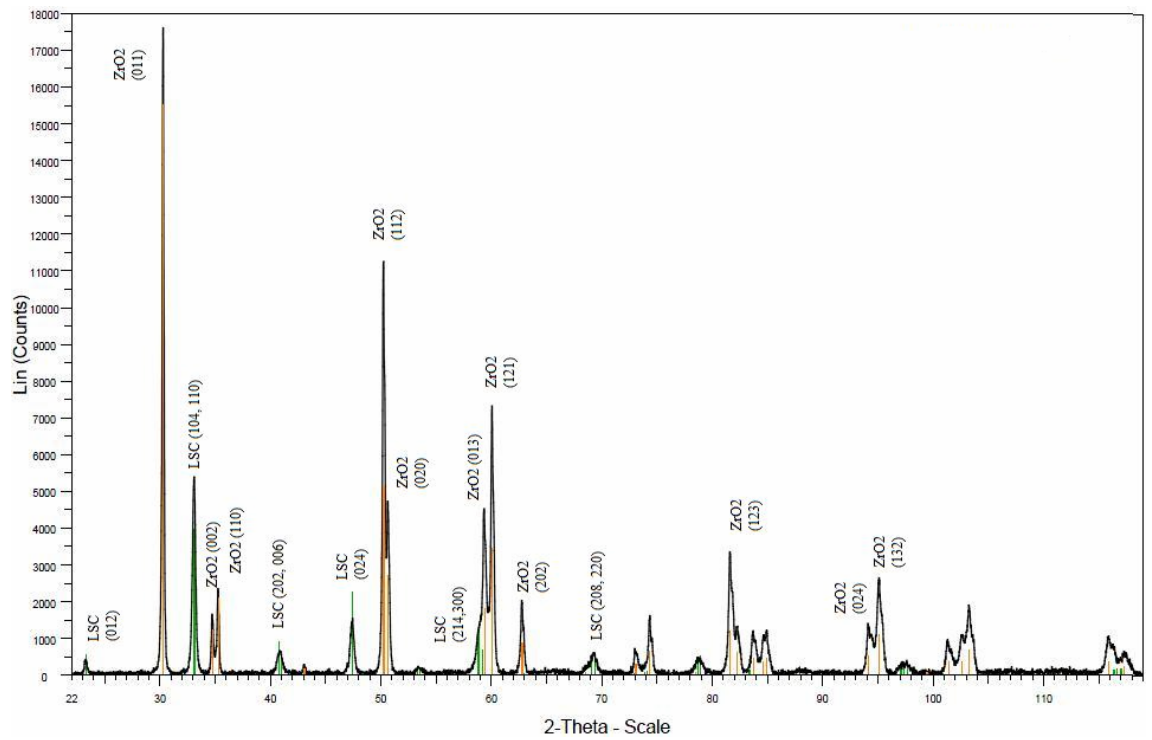Figure 4.23 XRD chart for sample C15

Figure 4.24 XRD chart for sample Z1
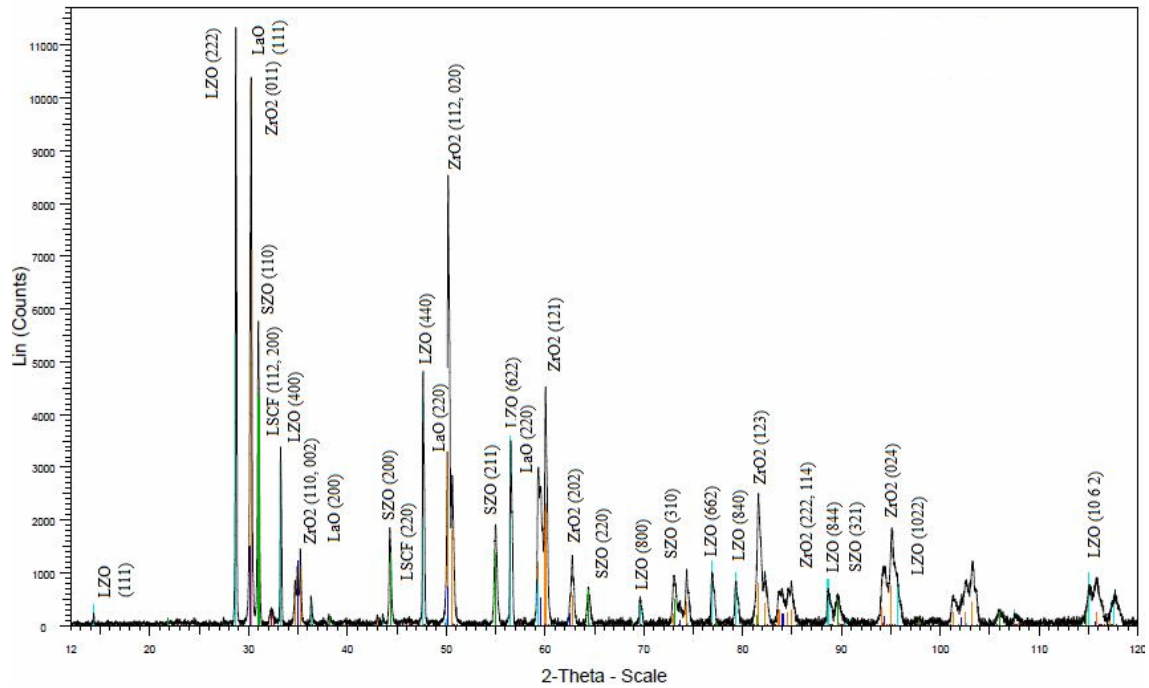
Figure 4.25 XRD chart for sample Z3

Figures 4.26 and 4.27 show high temperature X-ray analysis of samples prepared under the same conditions with Z1 and Z3. Again the peaks for the substrate ZrO_2 shifted to the left due to lattice expansion upon heating. Starting with 550 °C and higher formation of compounds like LSC and LSCF were observed following decomposition of salts in the coating. The sample heated at 1300 °C showed similar XRD pattern.

Figure 4.26. HTXRD analysis chart for sample with La$_{0.6}$Sr$_{0.4}$Co$_{0.8}$Fe$_{0.2}$O$_{3-\delta}$ coating on TZ-3Y substrate. Stronger peaks belong to ZrO$_2$ from the substrate
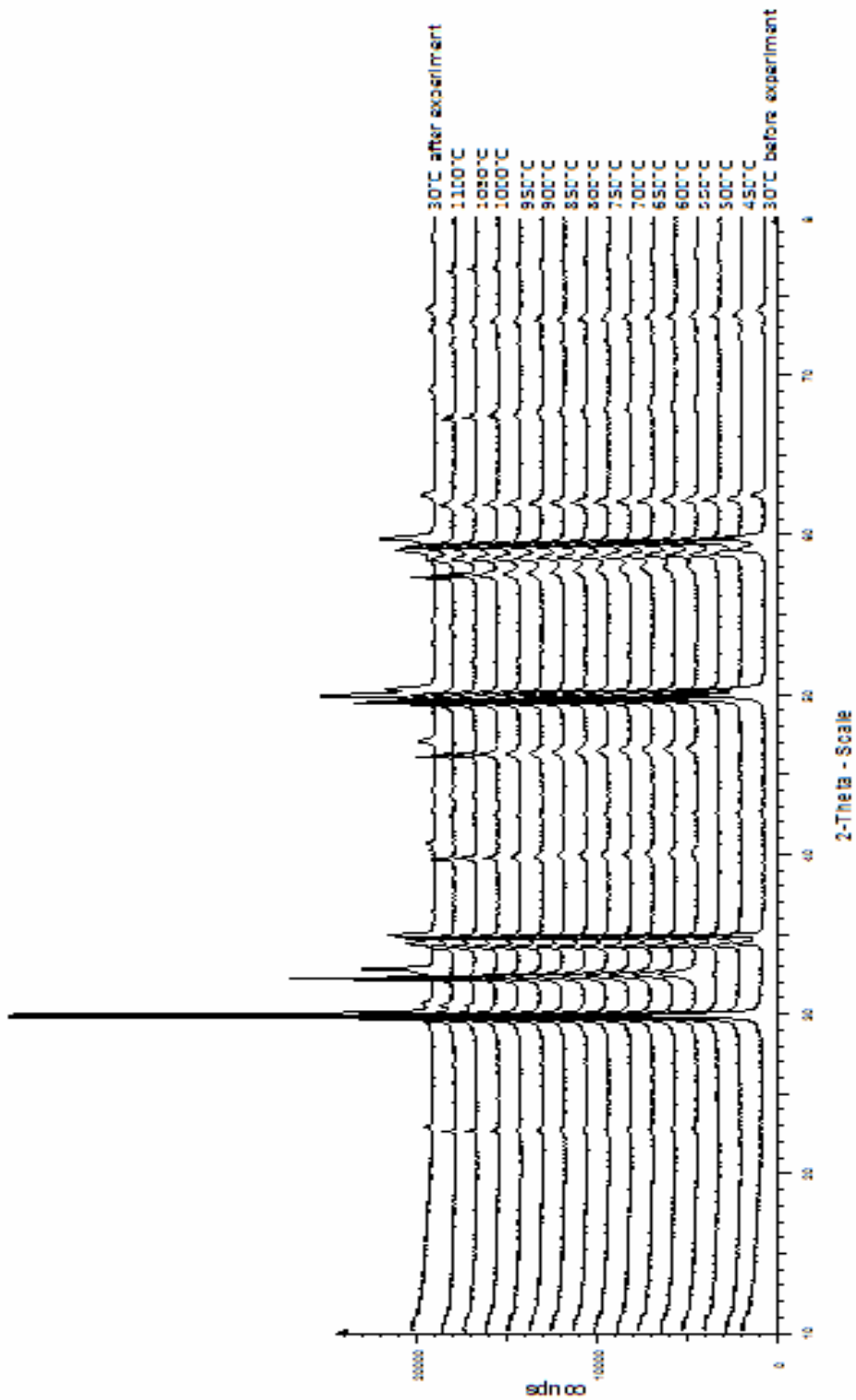
Figure 4.27. HTXRD analysis chart for sample with $La_{0.6}Sr_{0.4}Co_{0.8}Fe_{0.2}O_{3-\delta}$ coating on TZ-3Y substrate. Stronger peaks belong to ZrO_2 from the substrate

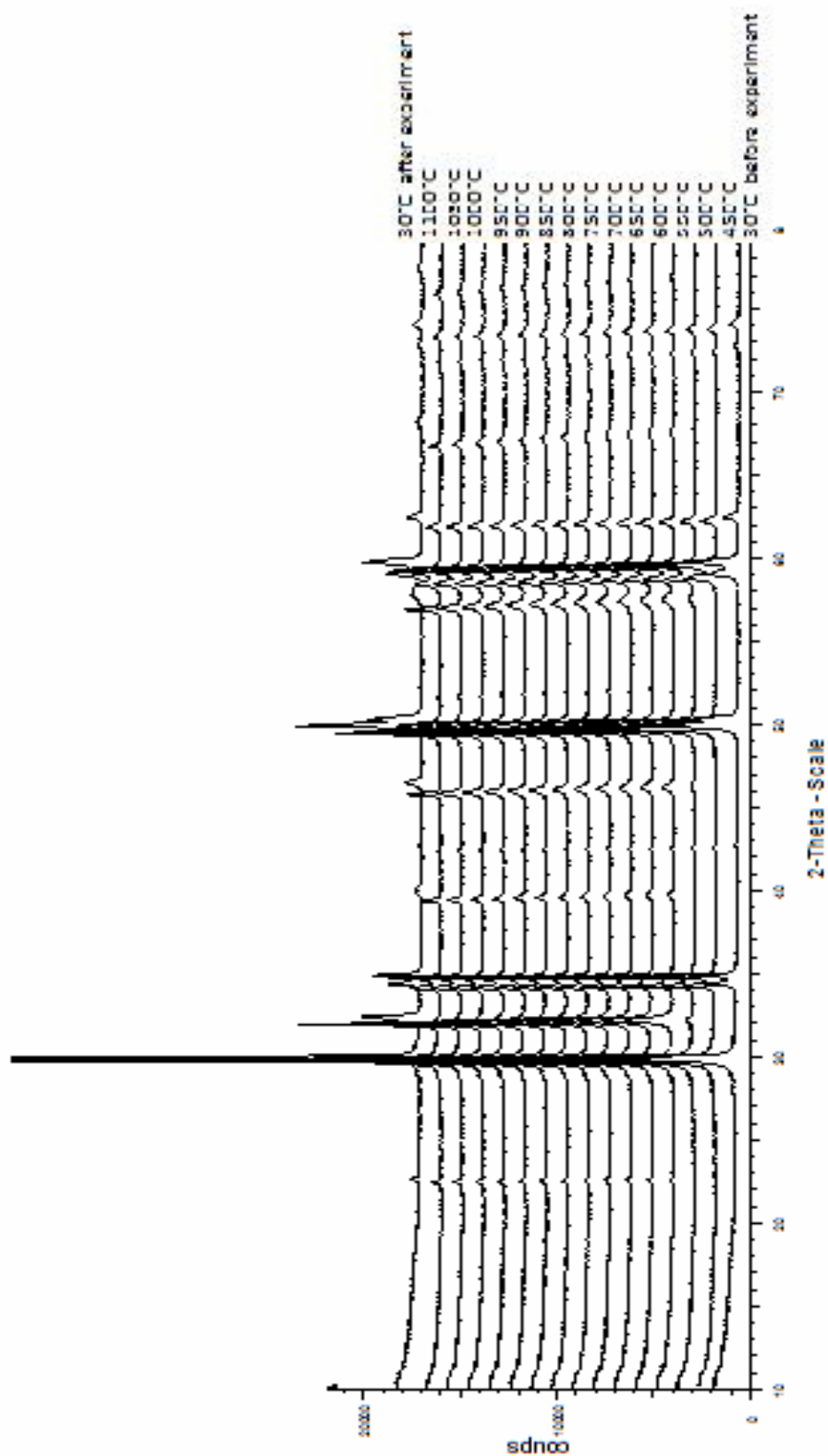In Figures 4.28 and 4.29, XRD analysis results of the $La_{0.6}Sr_{0.4}Co_{0.2}Fe_{0.8}O_3$ (LSCF-6428) coating on CGO substrate are shown. The samples were heat-treated at 900°C and 1300°C, respectively. At 900°C, CeO_2 and $Sr_{0.6}La_{0.4}FeO_3$ (SLF) compounds were found in sample C16. In additon to these compounds, $La_{0.6}Sr_{0.4}CoO_3$ compound was observed at 1300 °C in sample C18. Although $La_{0.6}Sr_{0.4}Co_{0.8}Fe_{0.2}O_3$ (LSCF-6482) compositon can be formed on CGO substrate, for example C15 sample, $La_{0.6}Sr_{0.4}Co_{0.2}Fe_{0.8}O_3$ (LSCF-6428) did not form on the same substrate for any of the temperatures. Iron ions were unable to get into the LSCF structure, but formed a separate iron-containing compound of SLF instead.

As far as the formation of the intended LSCF composition is concerned, sample C15 was the best one. None of the other samples was able to reach the expected LSCF composition.
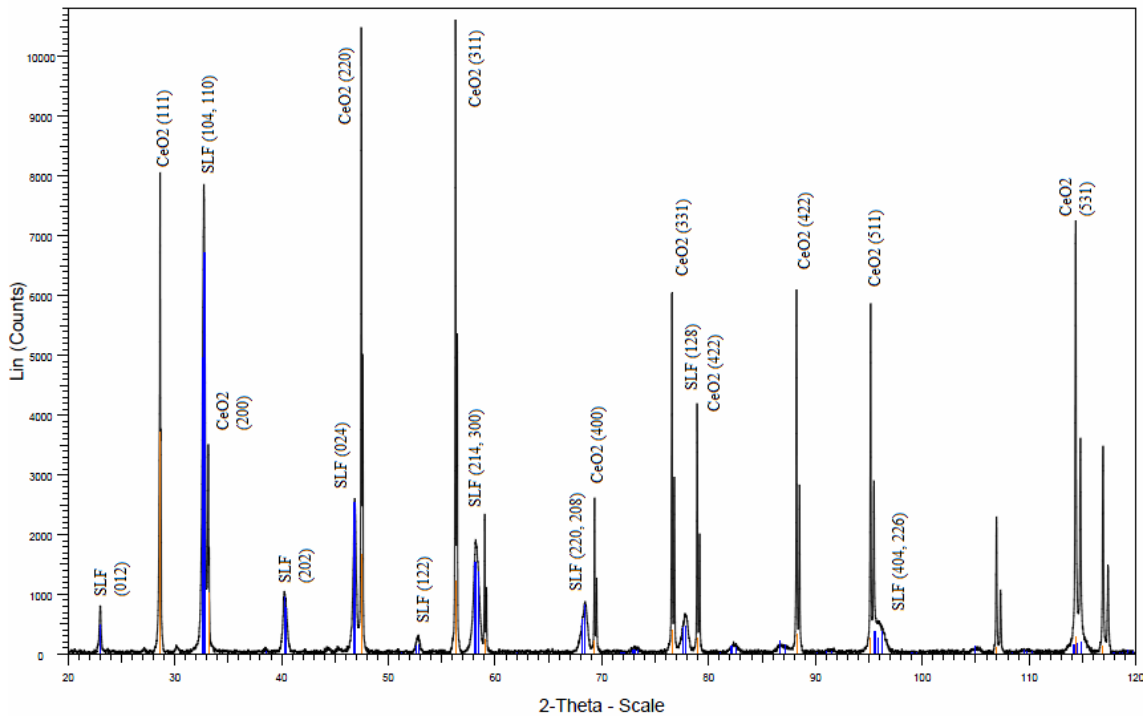

Figure 4.28. XRD chart for sample C16
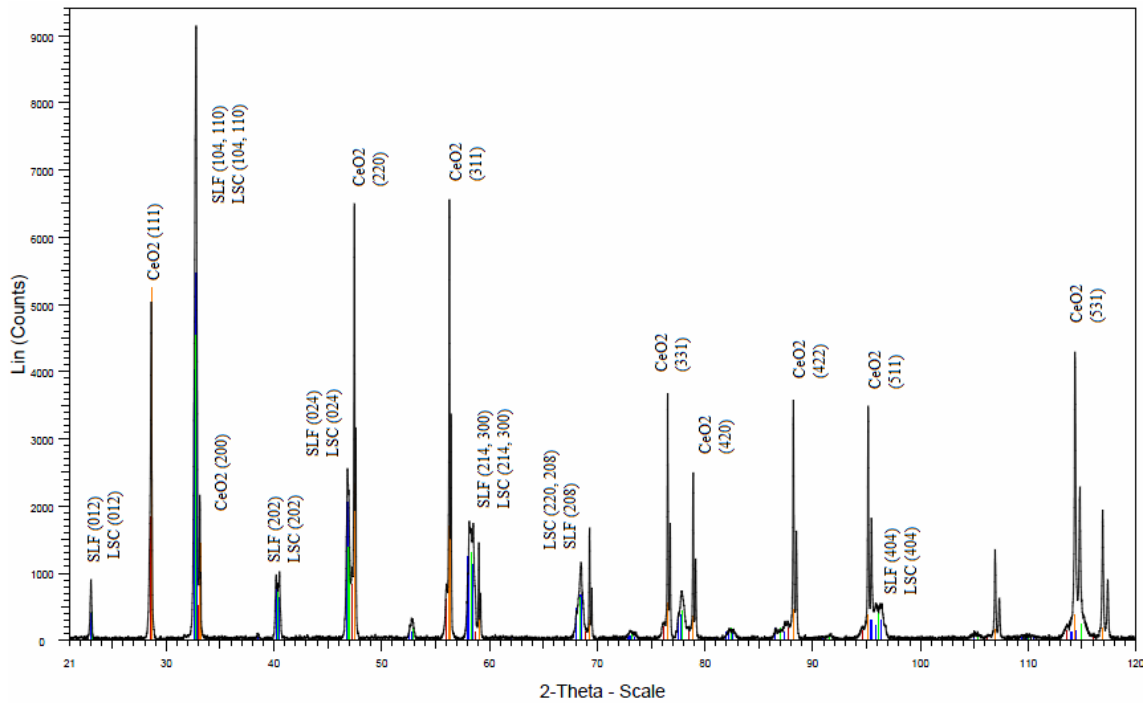
Figure 4.29. XRD chart for sample C18

Based on the information provided by the XRD analysis of zirconia substrates coated with LSCF zirconia was found to react with the coating upon the 900-1300 °C thermal treatment. When considering results of XRD analyses on CGO and TZ-3Y substrates, CGO appeared to be more appropriate than TZ-3Y. Because at high temperature, $La_{0.6}Sr_{0.4}Co_{0.8}Fe_{0.2}O_{3-\delta}$ film formed on CGO substrate, but $La_{0.6}Sr_{0.4}Co_{0.8}Fe_{0.2}O_{3-\delta}$ film formed with different composition ($La_{0.7}Sr_{0.3}Co_{0.3}Fe_{0.7}$) on TZ-3Y substrate. XRD analysis was not performed on samples Z4, Z5 and Z6 but the general trend is expected to follow the pattern observed for samples C13, C15, Z1 and Z3. Electrical measurements need to be performed to conductivity rank the substrates for their potential effectiveness.

CHAPTER 5

CONCLUSIONS

LSCF coating on CGO and TZ-3Y substrates was successfully accomplished. Initially, a solution with the correct stoichiometry for $La_{0.6}Sr_{0.4}Co_{0.8}Fe_{0.2}O_{3-\delta}$ (LSCF-6482) was prepared by dissolving mixtures of salts of $La(NO_3)_3.6H_2O$, $SrCl_2.6H_2O$, $Fe(NO_3)_3.9H_2O$, $Co(NO_3)_2.6H_2O$ in ethanol-water or butyl carbitol-ethanol solvents. Different compositions of solvent mixtures were tested. Electrical conductivities of the solutions were also measured to make sure that the salts were completely dissolved. An ESD (electrostatic spray deposition) setup was used to spray-coat the LSCF solutions on heated substrates. The ceramic samples were found to be successfully coated with good reticulated structure in most of the samples. Especially the samples coated at 15 mm distance, 0.7 ml/h of flow rate and 250 °C of substrate heating temperature were observed to be coated best. The coating layer was continuous over the surface of the substrate with a minimum thickness of 1μm when they were post heat treated at 900 °C. The substrate type did not make any difference on the coating structure. When this heat treatment temperature was increased to 1300 °C the coating was found to have a fully dense structure with no porosity. This dense structure was not amorphous but was crystalline as determined by XRD to be largely composed of crystals of LSCF-6482. TZ-3Y was found to react with the coating and to modify its composition to deviate from LSCF-6482. CGO substrate appeared to be better in terms of compatibility with the coating during thermal treatment step. Electrical measurements need to be done to reach conclusions about the potential service performance of the system.

It is suggested that electrical conductivity measurements be done on the samples. Another topic for potential future study is to study interface reactions between prepared LSCF coating and the substrate on furnace heated samples instead of ESD coated samples. Thermodynamic assessment of potential reactions between substrate and coating must be done to obtain predictive information about the suitability of different substrate and coating systems.

REFERENCES

Chen C. Thin Films Components For Lithium Ion Batteries. Ph.D. Delft University of Technology, Netherlands, **1998**.

EG&G Technical Services, Inc. *Fuel Cell Handbook*, 7th ed.; U.S. Department of Energy Office of Fossil Energy National Energy Technology Laboratory, West Virginia, **2004**.

Hoogers G. *Fuel Cell Technology Handbook*, 2nd.; CRC Press, **2003**.

ECN, Energy Research Centre of the Netherlands. http://www.ecn.nl (accessed 2010).

Huijmans J. P. P., Van Berkel F. P. F., Christie G.M. Intermediate Temperature SOFC-a Promise For the 21st Century. Journal of Power Sources **1998**, 71, 107-110.

Huijmans J. P. P. Ceramics In Solid Oxide Fuel Cells. Solid State & Materials Science. **2001**, 5, 317-323.

Ishihara T, Matsuda H. and Takita Y. Doped $LaGaO_3$ Perovskite Type Oxide as a New Oxide Ionic Conductor. *J. American Chem. Soc.*, **1994**, 116, 3801.

Jaworek A., Sobczyk A. T. Electrospraying Route to Nanotechnology: An overview *Journal of Electrostatics* **2008**, 66, 197-219.

Larminie J., Dicks A. Fuel Cell Systems Explained. John Wiley **2003**.

Marinha D., Rossignol, C.; Djurado, E. Influence of Electrospraying Parameters on the Microstructure of $La_{0.6}Sr_{0.4}Co_{0.2}Fe_{0.8}O_{3-\delta}$ Films for SOFCs. *Journal of Solid State Chemistry* **2009**, 182, 1742-1748.

Minh N. Q., Takahashi T. Science and Technology of Ceramic Fuel Cells *Elsevier Science* **1995**.

Neagu R. Elaboration de Films Minces d'electrolyte par une Technique Innovative: L'atomisation Electrostatique. Instıtut National Polytechnique de Grenoble **2005**.

Neagu R., Perednis D., Princivalle A., Djurado E. Influence of The Process Parameters   on the ESD Synthesis of Thin Film YSZ Electrolyte. *Solid State Ionics* **2006**, 177, 1981-1984.

Nguyen T., Djurado E. Deposition and Characterization of Nanocrystalline Tetragonal Zirconia Films Using Electrostatic Spray Deposition **2001**, 138, 191-197.

Nicolas J. D. Low Temperature Constrained Sintering of Cerium Gadolinium Oxide for Solid Oxide Fuel Cell Applications **2007**.

Petric A., Huang P., Tietz F. Evaluation of La- Sr-Co- Fe- O Perovskites for Solid Oxide Fuel Cell and Gas Preparation. *Solid State Ionics* **2000**, 135, 719-725.

Primdahl S., Sørensen B. F., Mogensen M. Effect of Nickel Oxide/ Yttria-Stabilized Zirconia Anode Precursor Sintering Temperature on the Properties of Solid Oxide Fuel Cells. *Journal of American Ceramic Society* **2000**, 83, 489-494.

Princivalle A., Perednis D., Neagu R. and Djurado E. Microstructural Investigations of Nanostructured La(Sr)MnO$_{3-\delta}$ Films Deposited by Electrostatic   Spray Deposition. *Chem. Mater.* **2004**, 16, 3733-3739.

Ramani V. Fuel Cells. Electrochemical Society Interface **2006**.

Rosa D. L., Massimiliano F. L., Monforte G., Antonucci V., Arico A. Comparison of The Electrochemical Properties of Intermediate Temperature Solid Oxide Fuel Cells Based on Protonic and Anionic Electrolytes. *Journal Application Electrochemistry*   **2009**, 39, 477-483.

Sammes N. Fuel Cell Technology: Reaching Towards Commercialization. *Springer* **2006**.

Siefert W. Corona spray pyrolysis: A New Coating Technique with an Extremely Enhanced Deposition Effciency. *Thin Solid Films* **1984**, 120, 267–274.

Singhal S. C., Kendall K. High Temperature Solid Oxide Fuel Cells: Fundamentals, Design and Application **2003**.

Somiya S. Handbook of Advanced Ceramics. Ceramic Fuel Cells; Fleig J., Kreuer K. D., Maier J.; Elsevier, 2003; Vol. 2.

Steele B. C. H. Materials for IT-SOFC Stacks 35 Years R&D: The Inevitability of Gradualness. *Solid State Ionics* **2000**, 134, 3-20.

Søcrensen B. *Hydrogen and Fuel cells*, illustrated ed.; Elsevier Academic Press **2005**.

Taniguchi I., Landschoot R. C. V., Schoonman J. Fabrication of $La_{1-x}Sr_xCo_{1-y}Fe_yO_3$ Thin Films by Electrostatic Spray Deposition **2003**, 156, 1-13.

Tietz F., Mai A., Stöver D. From Powder Properties to Fuel Cell Performance- A Holistic Approach for SOFC Cathode Development. *Solid State Ionics* **2008**, 179, 1509-1515.

Venkatasubramanian V. Fuel Cells. Ph.D. Indian Institute of Technology, Madras, India, **2003**.

Tosoh Corporation, The Chemistry of Innovation, www.tosoh.com (accessed 2010).

Wilhelm O., Pratsinis S. E., Perednis D., Gauckler L. J. Electrospray and Pressurized Spray Deposition of Yttria- Stabilized Zirconia Films **2005**, 479, 121-129.

Yamamoto O, Arati Y, Takeda Y, Imanishi N, Mizutani Y, Kawai M and Nakamura Y. Electrical Conductivity of Stabilized Zirconia with Ytterbia and Scandia *Solid State Ionics* **1995**, 79, 137–142.

Yashima M., Kamioka T. Neutron Diffraction Study of The Perovskite-type Lanthanum Cobaltite La$_{0.6}$Sr$_{0.4}$Co$_{0.8}$Fe$_{0.2}$O$_{3-\delta}$ at 1260 °C and 394 °C. *Solid State Ionics* **2008**, 178, 1939-1943.